Journal of Physical and Chemical Reference Data

Network-Based Design of Near-Infrared Lamb-Dip Experiments and the Determination of Pure Rotational Energies of $H_2{}^{18}O$ at kHz Accuracy

Cite as: J. Phys. Chem. Ref. Data **50**, 023106 (2021); https://doi.org/10.1063/5.0052744
Submitted: 01 April 2021 . Accepted: 14 May 2021 . Published Online: 15 June 2021

Meissa L. Diouf, Roland Tóbiás, Irén Simkó, Frank M. J. Cozijn, Edcel J. Salumbides, Wim Ubachs, and Attila G. Császár

Journal of Physical and Chemical Reference Data ARTICLE scitation.org/journal/jpr

Network-Based Design of Near-Infrared Lamb-Dip Experiments and the Determination of Pure Rotational Energies of $H_2^{18}O$ at kHz Accuracy

Cite as: J. Phys. Chem. Ref. Data 50, 023106 (2021); doi: 10.1063/5.0052744
Submitted: 1 April 2021 • Accepted: 14 May 2021 •
Published Online: 15 June 2021

Meissa L. Diouf,[1] Roland Tóbiás,[2] Irén Simkó,[3] Frank M. J. Cozijn,[1] Edcel J. Salumbides,[1] Wim Ubachs,[1,a)] and Attila G. Császár[4,b)]

AFFILIATIONS

[1]Department of Physics and Astronomy, LaserLaB, Vrije Universiteit, De Boelelaan, 1081 HV Amsterdam, The Netherlands
[2]MTA-ELTE Complex Chemical Systems Research Group, P.O. Box 32, H-1518 Budapest 112, Hungary
[3]Institute of Chemistry, ELTE Eötvös Loránd University, Pázmány Péter sétány 1/A, H-1117 Budapest, Hungary
[4]Institute of Chemistry, ELTE Eötvös Loránd University, Pázmány Péter sétány 1/A, H-1117 Budapest, Hungary and MTA-ELTE Complex Chemical Systems Research Group, P.O. Box 32, H-1518 Budapest 112, Hungary

[a)]**Electronic mail:** w.m.g.ubachs@vu.nl
[b)]**Author to whom correspondence should be addressed:** attila.csaszar@ttk.elte.hu

ABSTRACT

Taking advantage of the extreme absolute accuracy, sensitivity, and resolution of noise-immune-cavity-enhanced optical-heterodyne-molecular spectroscopy (NICE-OHMS), a variant of frequency-comb-assisted Lamb-dip saturation-spectroscopy techniques, the rotational quantum-level structure of both nuclear-spin isomers of $H_2^{18}O$ is established with an average accuracy of 2.5 kHz. Altogether, 195 carefully selected rovibrational transitions are probed. The ultrahigh sensitivity of NICE-OHMS permits the observation of lines with room-temperature absorption intensities as low as 10^{-27} cm molecule^{-1}, while the superb resolution enables the detection of a doublet with a separation of only 286(17) kHz. While the NICE-OHMS experiments are performed in the near-infrared window of 7000–7350 cm^{-1}, the lines observed allow the determination of all the pure rotational energies of $H_2^{18}O$ corresponding to J values up to 8, where J is the total rotational quantum number. Both network and quantum theory have been employed to facilitate the measurement campaign and the full exploitation of the lines resolved. For example, to minimize the experimental effort, the transitions targeted for observation were selected via the spectroscopic-network-assisted precision spectroscopy (SNAPS) scheme built upon the extended Ritz principle, the theory of spectroscopic networks, and an underlying dataset of quantum chemical origin. To ensure the overall connection of the ultraprecise rovibrational lines for both nuclear-spin isomers of $H_2^{18}O$, the NICE-OHMS transitions are augmented with six accurate microwave lines taken from the literature. To produce absolute *ortho*-$H_2^{18}O$ energies, the lowest *ortho* energy is determined to be 23.754 904 61(19) cm^{-1}. A reference, benchmark-quality line list of 1546 transitions, deduced from the ultrahigh-accuracy energy values determined in this study, provides calibration standards for future high-resolution spectroscopic experiments between 0–1250 and 5900–8380 cm^{-1}.

Key words: benchmark line list; $H_2^{18}O$; NICE-OHMS; precision spectroscopy; rotational energies; saturation spectroscopy; SNAPS.

CONTENTS

List of Tables

List of Figures

1. Introduction

Detailed analysis of the spectra of water vapor, the most important greenhouse gas in the atmosphere of the Earth, has been at the center of (ultra)high-resolution molecular spectroscopy for many decades.[1–8] During this time, ever-improving techniques have been devised to resolve spectral features in diverse environments and determine the line parameters (e.g., positions, intensities, and shapes, as well as cross sections and collisional parameters) with rapidly increasing accuracy and coverage. These spectroscopic results, related mostly to the electronic ground state of water, have been collated into popular spectroscopic databases, such as HITRAN (HIgh-resolution TRANsmission molecular absorption database).[9] HITRAN2016, for example, contains more than 300 000 water lines, nearly 40 000 of which correspond to the second most abundant isotopologue of water, $H_2{}^{18}O$, with a natural terrestrial abundance of 0.2%. These water datasets are utilized by a large number of scientists and engineers, including modelers of atmospheric chemistry, combustion systems, exoplanets, and cool stars. In cases when lines of the main isotopologue are too strong, lines of less-abundant isotopologues are used to trace the chemical environment, e.g., in outer space, while in radio astronomy, $H_2{}^{18}O$ transitions are employed to assess isotopic ratios in the interstellar medium.[10]

Several microwave,[11–13] terahertz,[14–17] as well as far- and mid-infrared[18–23] studies have been conducted to observe purely rotational transitions of $H_2{}^{18}O$. Naturally, an even larger number of papers have been dedicated to record vibration-changing lines involving high-lying vibrational states,[24–31] whereby the lower quantum states of the transitions are mostly determined by pure rotational lines. The experimental results reported in articles dealing with infrared transitions are typically based on linear absorption, producing Doppler-broadened line shapes with a line-position uncertainty of 3–300 MHz.

A new scientific era arrived when experimental protocols employing optical frequency-comb (OFC) lasers were introduced.[32,33] The OFC is linked to the spectroscopy laser so as to interrogate the spectra of gas-phase molecules with sub-MHz accuracy.[34–36] Despite the promise of these new techniques, up until now, only two articles[37,38] dealing with sub-Doppler laser spectroscopy of $H_2{}^{18}O$ have been published, reporting 18 lines with 30 kHz accuracy.

OFCs are often coupled with cavity enhancement;[39,40] this is the case for the noise-immune-cavity-enhanced optical-heterodyne-molecular spectroscopy (NICE-OHMS).[41–45] In the previous sub-Doppler studies of $H_2{}^{18}O$ mentioned,[37,38] Lamb dips calibrated with 30 kHz accuracy have been recorded. The narrow line shapes result in an increase in the accuracy of the line-center determination, generally by a factor of a thousand or so, reducing the experimental uncertainty from the MHz to the kHz regime.

Some ten years ago, after collecting all the experimental lines from the literature, an IUPAC-sponsored effort resulted in lists of observed transitions and empirical energy levels for $H_2{}^{18}O$.[2,3] These large datasets have recently been updated, significantly extended, and integrated into the W2020 database.[7,8] The empirical energy values of the original IUPAC dataset served as a basis for the development of first-principles line lists,[46,47] with accurate Einstein-*A* coefficients and line intensities. Together with line positions derived from W2020 energy levels, these data were employed during this study to guide the selection of lines for measurement.

In this study, the NICE-OHMS intracavity absorption method is applied, in combination with OFC-linked laser spectroscopy, to record saturated spectra of the $H_2{}^{18}O$ species. The Lamb-dip measurements are conducted in the near infrared in a systematic fashion; the lines chosen for measurement have been selected via the Spectroscopic-Network-Assisted Precision Spectroscopy (SNAPS) scheme,[48] with the aim to determine ultraprecise pure rotational energies within the ground vibrational state of $H_2{}^{18}O$. Determining a large number of pure rotational energies is a significant achievement since these quantum states are all hubs in the spectroscopic network (SN) of $H_2{}^{18}O$;[49–52] thus, they are the lower states of a huge number of

transitions measured in absorption by a number of different experimental techniques. As a useful by-product, energy levels with high-lying vibrational parents are also obtained. Based on the SNAPS energies, a benchmark-quality reference line list is constructed, providing frequency standards for a number of future high-resolution spectroscopic measurements.

2. Methods and Data Treatment

2.1. NICE-OHMS spectroscopy

A NICE-OHMS apparatus,[44,48] shown schematically in Fig. 1, has been deployed to detect saturated absorption lines of $H_2^{18}O$ in the near-infrared region. In our setup, an infrared diode laser functioning at 1.4 μm is used along with a high-finesse cavity. This laser is modulated at 305 MHz, equivalent to the free spectral range (FSR) of the cavity, for generating sideband signals and at 20 MHz for the cavity-lock via a Pound–Drever–Hall (PDH) stabilization scheme. Thanks to the highly reflective mirrors, the intracavity power can be increased up to 150 W. This high upper power limit enabled the saturation of several rovibrational transitions for $H_2^{18}O$, inducing extremely narrow Lamb-dip profiles. In addition, one of the mirrors is dithered at a low frequency of 405 Hz. The spectroscopic signal is treated and demodulated by a powerful lock-in system (Zurich Instruments, HF2LI). A high-stability OFC, disciplined by a cesium atomic clock, is also incorporated in the NICE-OHMS spectrometer to stabilize the infrared laser and to obtain sub-kHz accuracy on the frequency axis.

Due to the long-term stabilization of the cavity and the demodulated signal, NICE-OHMS is a highly sensitive method, while its accuracy is warranted by its lock to the OFC. The Lamb-dip signals exhibit very narrow profiles with widths of 400–800 kHz (full width at half-maximum). The linewidth is governed by power and pressure broadening, as well as by the transit time of the molecules across the laser beam.

The individual line centers are somewhat shifted by the laser power and the vapor pressure within the water cell. The vapor pressure is controlled by injecting, using an inlet valve, an enriched $H_2^{18}O$ sample (Sigma-Aldrich, St. Louis, MO, 97% ^{18}O isotopic purity). To overcome the effect of outgassing from the cavity walls, the absorption cell is directly linked to a vacuum pump removing any excess of $H_2^{18}O$ molecules. Hence, the spectroscopic recordings are performed under slow but steady gas flows, at pressures in the range of 0.03–1.0 Pa, measured by a capacitance pressure gauge. Collisional shifts are also studied experimentally, facilitating an extrapolation to zero pressure.

Limited by the operation range of the diode laser, the reflectivity of the cavity mirrors, and the transmission of some optical elements, our NICE-OHMS setup works in the wavenumber interval of 7000–7350 cm^{-1}. By varying the intracavity power, transitions with $A_E = 10^{-4}$–10^{2} s^{-1} and $S = 10^{-27}$–10^{-20} cm molecule^{-1} can be resolved in saturation with a sufficient signal-to-noise ratio (SNR) and negligible power broadening, where A_E is the Einstein-A coefficient, while S means the line intensity without abundance scaling. These constraints on the three quantities, called primary line parameters in the remainder of this paper, dictate which lines can be effectively probed and included in the SNAPS scheme.

2.2. The SNAPS scheme

The near-infrared transitions of $H_2^{18}O$ observable with our NICE-OHMS setup were selected via the SNAPS procedure[48] to maximize the accurate spectroscopic information that can be extracted from the newly probed lines. While SNAPS was discussed in detail before,[48] it is briefly outlined here for readability and completeness.

During the SNAPS design, one should (a) determine paths and cycles (see Fig. 2) involving accurate literature transitions as well as target lines in the accessible range of the primary line parameters, (b) proceed with the recording of the targeted transitions selected based on the knowledge of these paths and cycles, and (c) evaluate the paths and cycles of the new and literature transitions to estimate accurate energy differences and their uncertainties as well as to verify the internal accuracy of the experiments. Despite the fact that SNAPS is built upon the use of network theory, it is a black-box-type strategy, and its output requires only the understanding of Fig. 2 (for interested readers, a concise summary of network theory related to high-resolution spectroscopy is given in Supplementary Note 1 of Ref. 48).

As to the primary line parameters of the target transitions, (a) the approximate wavenumbers were calculated from the W2020 energies of Ref. 8 with an uncertainty of 10^{-4}–10^{-2} cm^{-1} in the 7000–7350 cm^{-1} window; (b) the Einstein-A coefficients, A_E,

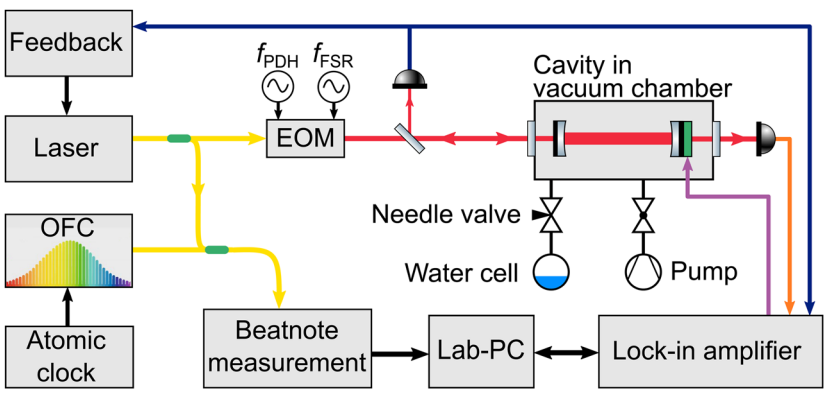

FIG. 1. Schematic layout of the NICE-OHMS setup.

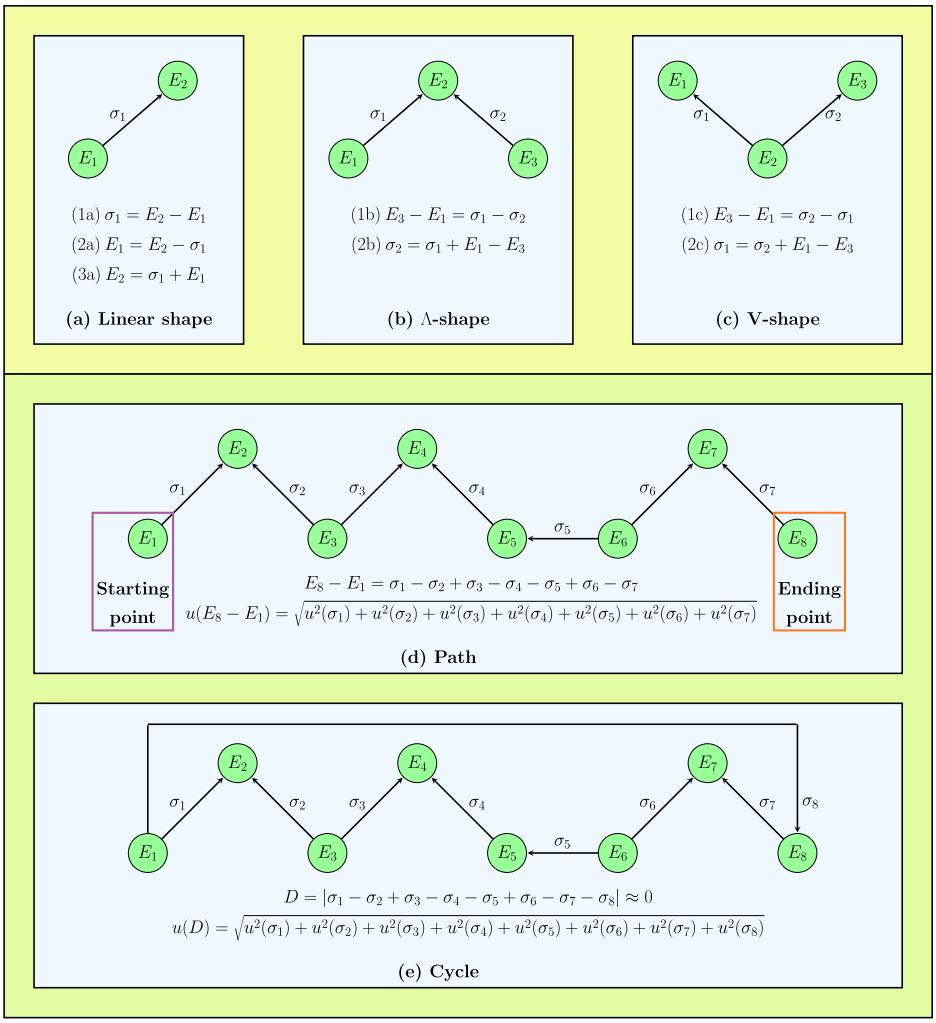

FIG. 2. Traditional and generalized connection schemes characterizing spectroscopic measurements. Nodes and edges of the connection schemes (a)–(e) are quantum states with energies E_i and transitions with wavenumbers σ_i, respectively. Equation (1a) corresponds to the definition of the Ritz principle. Panels (b) and (c) are connection schemes widely utilized by spectroscopists, usually referred to as combination differences. In an analogous way, extended connections can also be defined, involving not two but more transitions. Panel (d) illustrates a path (a series of connected, unrepeated lines and states), while panel (e) exhibits a cycle (a sequence of linked transitions and energy levels, where each energy level is connected to two neighboring states). The connection schemes mentioned, linear, Λ, and V, are themselves examples of paths. Employing the Ritz principle in a successive fashion, the energy differences between any node pairs of a path can be determined straightforwardly. If the starting point of the path is the lowest energy level attainable from the ending point through paths, then $E_8 - E_1$ is defined as the relative energy of the ending point. In the case that the starting point is the rovibrational ground state of the species under study (i.e., $E_1 = 0$), $E_8 - E_1$ gives an estimate for the absolute energy of the ending point. Knowledge of the $u(\sigma_i)$ wavenumber uncertainties yields the uncertainty of the $E_8 - E_1$ difference, expressed from the law of uncertainty propagation (as long as measurement errors are uncorrelated and they have zero expected values). Cycles demonstrate the internal accuracy of their transitions: in favorable cases, $D \le t_{crit}u(D)$, where D is the discrepancy (the absolute signed sum of the observed wavenumbers) of the cycle with its $u(D)$ uncertainty and $t_{crit} = 2$ assuring a 95% confidence level.

were adopted from Ref. 47; and (c) the line intensities were calculated according to Eq. (3) of Ref. 55. Even though the accuracy of the W2020 positions was sufficient to detect the majority of the target transitions, the very weak lines (with $S < 1 \times 10^{-25}$ cm molecule^{-1} or with $A_E < 1 \times 10^{-3}$ s^{-1}) required much smaller uncertainties for the initial wavenumbers to avoid extreme scanning times.

A solution found to the refinement of the starting wavenumbers involves building a Λ-shape connection [see Fig. 2(b)], whereby one of the lines is easily observable (has optimal intensity and Einstein-A coefficient), while the other is the weak transition. After recording the stronger signal (σ_1) and employing accurate lower-state energies (E_1 and E_3, see Fig. 2), an improved initial position (σ_2) can be obtained for the weaker transition via Eq. (2b) of Fig. 2. [High-accuracy lower-state energies can be extracted, e.g., from an effective Hamiltonian (EH) fit to the intermediate transition dataset.] Utilizing the (two or three orders of magnitude) more precise σ_2 position, the weaker line can be detected within reasonable time limits. This kind of wavenumber adjustment is called here Λ-correction. Typical short cycles and paths formed during

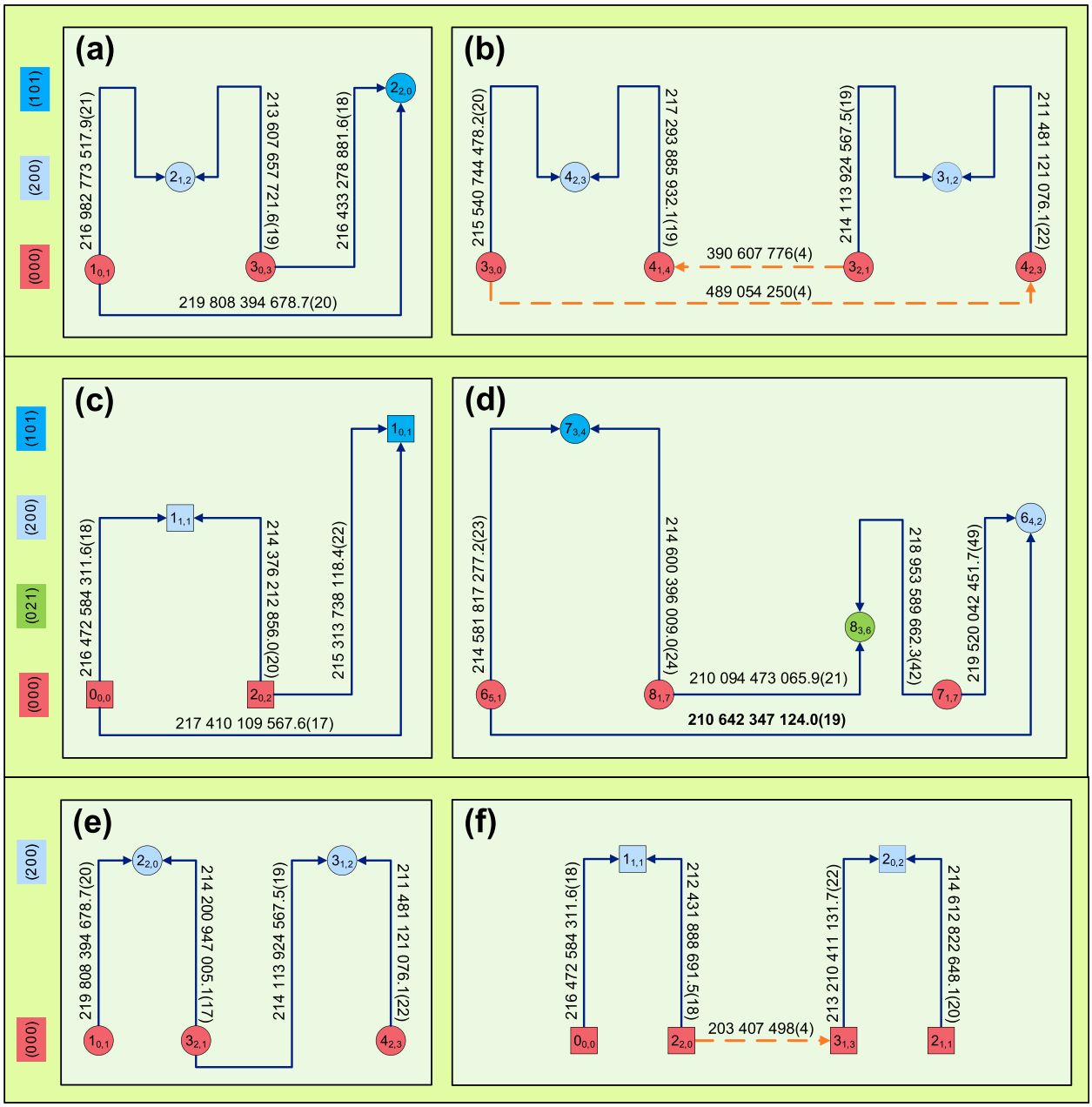

FIG. 3. Typical short cycles and paths formed during the SNAPS analysis of $H_2{}^{18}O$. The color codes and symbols of this figure are explained in Figs. 4 and 5. Panels (a)/(c) and (b)/(d) exhibit four- and six-membered cycles, respectively. Each transition is associated with its frequency, in kHz, and the uncertainty of the last few frequency digits, given in parentheses. Successive application of the Ritz principle [see the formulas of Fig. 2(e)] yields the following discrepancies: 0.8(39) [panel (a)], 11.5(69) [panel (b)], 6.4(39) [panel (c)], and 0.5(39) kHz [panel (d)]. All these cycles obey the relation $D \leq t_{crit}u(D)$ (see also the caption to Fig. 2). The line with boldfaced frequency was first confused with a close-lying $H_2{}^{16}O$ transition [(0 2 1)$6_{2,5} \leftarrow$ (0 0 0)$5_{2,4}$], exhibiting a line center of 210 642 354 724.6(50) kHz and leading to an unrealistically large discrepancy of 7600.7(91) kHz. Panels (e) and (f) are example paths for the determination of relative energies of $H_2{}^{18}O$. Repeated utilization of the Ritz principle [see the formulas of Fig. 2(d)] provides relative energies of 274.865 192 41(13) cm^{-1} [corresponding to 8 240 251 165.0(39) kHz] and 94.788 628 80(19) cm^{-1} [that is, 2 841 691 601.7(56) kHz] for (0 0 0)$4_{2,3}$ and (0 0 0)$2_{1,1}$, respectively. The energy values of the intermediate states can also be deduced from these paths.

the SNAPS analysis of $H_2^{18}O$ are depicted in Fig. 3; the interested reader should consult this figure to gain further insight into the utility of elements of SN theory to high-resolution spectroscopy.

Relying on the SNAPS approach extended with the Λ-correction scheme, and utilizing six accurate pure rotational transitions from the literature,[13] 195 near-infrared lines of $H_2^{18}O$ were selected and then

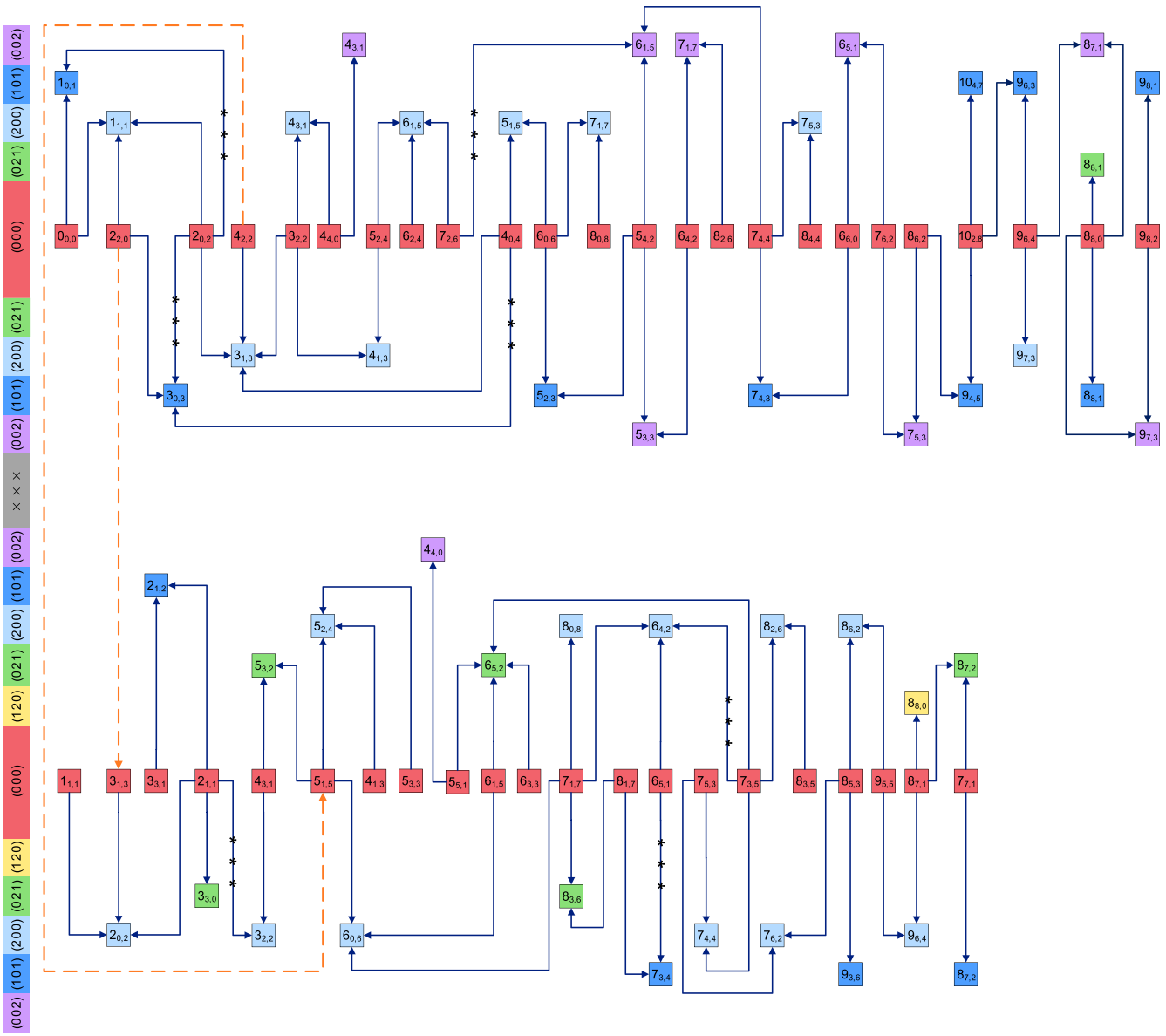

FIG. 4. Graphical representation of all the precision lines recorded for *para*-$H_2{}^{18}O$. The rovibrational eigenstates are characterized with the ordered sextuple $(v_1\ v_2\ v_3)J_{K_a,K_c}$, where $(v_1\ v_2\ v_3)$ is composed of the vibrational normal-mode quantum numbers according to the Mulliken convention,[53] while J_{K_a,K_c} are the standard asymmetric-top rotational quantum numbers.[54] Lines with lower states having even and odd K_c values, forming two subcomponents (p^+ and p^-, respectively) are drawn separately. Within the subcomponents, the *para* energy levels, those with even $v_3 + K_a + K_c$ values and symbolized with squares, are arranged palindromically in increasing (upper half) and decreasing (lower half) energy order of their vibrational parents and are denoted with distinct colors. The J_{K_a,K_c} rotational assignment is marked individually for each state, while the $(v_1\ v_2\ v_3)$ vibrational quantum numbers[53] are specified in the left-side color legend. The six vibrational bands lie in the $P = 0$ [(0 0 0)] and $P = 4$ [(1 2 0), (0 2 1), (2 0 0), (1 0 1), and (0 0 2)] polyads, where $P = 2v_1 + v_2 + 2v_3$ is the polyad number. The blue arrows indicate the outcome of the present NICE-OHMS measurements, while those with dashed orange arrows are taken from Ref. 13. The frequencies of the two literature lines are as follows: 203 407 498(4) kHz [(0 0 0)$3_{1,3}$ ← (0 0 0)$2_{2,0}$] and 322 465 122(2) kHz [(0 0 0)$5_{1,5}$ ← (0 0 0)$4_{2,2}$]. The non-starred arrows specify lowest-uncertainty unique paths from (0 0 0)$0_{0,0}$ to all the other energy levels of this figure. Each starred transition defines a cycle with the unique path of non-starred lines between its lower and upper states. Throughout this paper, the rovibrational transitions are designated with $(v_1'\ v_2'\ v_3')J'_{K_a',K_c'} \leftarrow (v_1''\ v_2''\ v_3'')J''_{K_a'',K_c''}$, where $'$ and $''$ refer to the upper and lower states, respectively.

detected via NICE-OHMS measurements. Graphical representations of these accurate $H_2{}^{18}O$ transitions, old and new, are displayed in Figs. 4 and 5 for *para*- and *ortho*-$H_2{}^{18}O$, respectively. All the newly measured lines, with their assignments, are listed in Table 1.

It is important to emphasize that within the two components, corresponding to the two nuclear-spin isomers of $H_2{}^{18}O$, two poorly connected subnetworks ("subcomponents") can be seen in Figs. 4 and 5. The p^+, p^-, o^+, and o^- subcomponents pertain to the $(p'', q'') = (+1, +1)$,

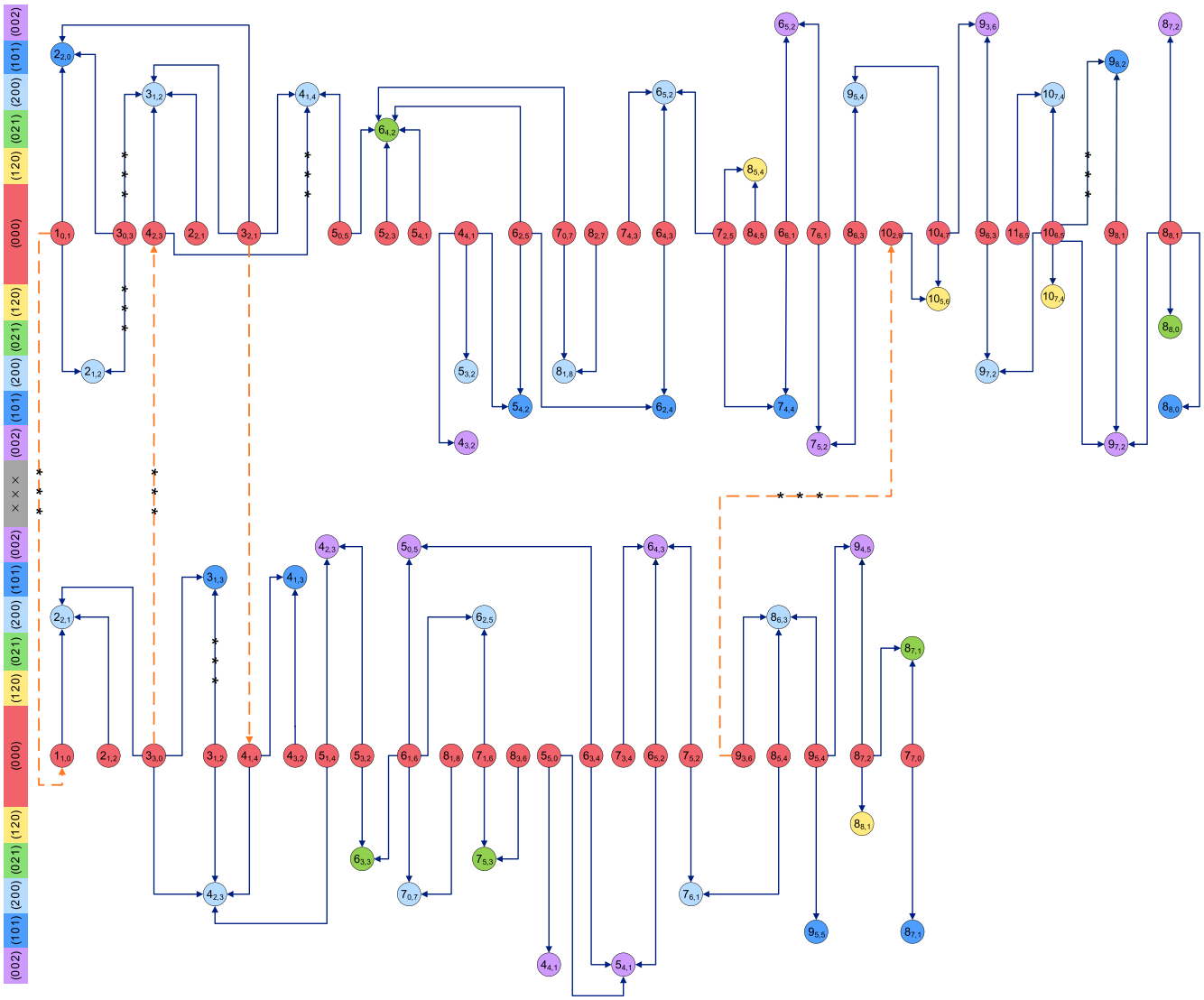

FIG. 5. Graphical representation of all the precision lines recorded for *ortho*-$H_2{}^{18}O$. The arrangement of the energy levels and the lines, as well as the formalism employed, is analogous to that of Fig. 4, with the exception that the *ortho* levels, characterized by odd $v_3 + K_a + K_c$ values, are denoted with circles rather than squares. The NICE-OHMS transitions are concentrated in two subcomponents (o^+ and o^-, whose lower states are identified with even and odd K_c values, respectively), which are linked with the following transitions:[13] 253 913 309(7) kHz [(0 0 0)$10_{2,9}$ ← (0 0 0)$9_{3,6}$], 390 607 776(4) kHz [(0 0 0)$4_{1,4}$ ← (0 0 0)$3_{2,1}$], 489 054 250(4) kHz [(0 0 0)$4_{2,3}$ ← (0 0 0)$3_{3,0}$], and 547 676 470(15) kHz [(0 0 0)$1_{1,0}$ ← (0 0 0)$1_{0,1}$]. The non-starred lines provide lowest-uncertainty unique paths from (0 0 0)$1_{0,1}$ to all the other energy levels of this figure. Moreover, every starred arrow forms a cycle with the unique path of non-starred lines between its lower and upper levels.

(−1, +1), (+1, −1), (−1, −1) pairs, respectively, where $p'' = (-1)^{K_c''}$ and $q'' = (-1)^{v_3''+K_a''+K_c''}$, while v_3'', K_a'', and K_c'' are lower-state quantum numbers (see also the caption of Fig. 4). While the *para* ($q'' = +1$) component cannot be linked experimentally with the *ortho* ($q'' = -1$) one, the $p'' = 1$ and $p'' = -1$ subcomponents (p^+/p^- and o^+/o^-) can be connected with pure rotational lines,[13] though they cannot be linked with dipole-allowed vibration-altering transitions. One should also realize that these kHz-accuracy rotational lines are fully disconnected in themselves, hindering their independent utilization in the derivation of accurate rovibrational energies.

2.3. Variational nuclear-motion computations

Due to their extremely low intensities ($S < 10^{-30}$ cm molecule^{-1}), no *ortho-para* transitions of $H_2^{18}O$ have been observed (see Ref. 56, dealing with $H_2^{16}O$). Therefore, the energy of the *ortho* states relative to the *para*-type rovibrational ground state cannot be derived solely from experiment. A possible way to link the *ortho* and *para* components is to find a path, from (0 0 0)$0_{0,0}$ to (0 0 0)$1_{0,1}$, which comprises highly accurate experimental transitions and a virtual line between nearly degenerate *para* and *ortho* levels.[4,48] Adjacent $(v_1\ v_2\ v_3)J_{J,0/1}$ pairs with fairly large J values are the most suitable

TABLE 1. The list of experimental transition frequencies of $H_2^{18}O$ measured in the present study[a]

No.	Assignment	Frequency (kHz)
1	$(2\ 0\ 0)3_{2,2} \leftarrow (0\ 0\ 0)4_{3,1}$	209 868 445 082.8 ± 2.6
2	$(0\ 2\ 1)7_{5,3} \leftarrow (0\ 0\ 0)8_{3,6}$	209 882 452 997.8 ± 2.2
3	$(2\ 0\ 0)6_{1,5} \leftarrow (0\ 0\ 0)7_{2,6}$	209 899 496 368.1 ± 1.7
4	$(0\ 0\ 2)7_{1,7} \leftarrow (0\ 0\ 0)8_{2,6}$	209 921 492 496.8 ± 3.6
5	$(2\ 0\ 0)7_{0,7} \leftarrow (0\ 0\ 0)8_{1,8}$	210 061 488 259.7 ± 1.9
6	$(2\ 0\ 0)7_{1,7} \leftarrow (0\ 0\ 0)8_{0,8}$	210 068 848 907.1 ± 2.2
7	$(2\ 0\ 0)3_{1,3} \leftarrow (0\ 0\ 0)4_{2,2}$	210 077 627 952.7 ± 1.9
8	$(2\ 0\ 0)10_{7,4} \leftarrow (0\ 0\ 0)11_{6,5}$	210 082 791 341.3 ± 5.2
9	$(0\ 2\ 1)8_{3,6} \leftarrow (0\ 0\ 0)8_{1,7}$	210 094 473 065.9 ± 2.1
10	$(1\ 2\ 0)10_{5,6} \leftarrow (0\ 0\ 0)10_{4,7}$	210 102 547 824.2 ± 3.9
11	$(1\ 2\ 0)8_{5,4} \leftarrow (0\ 0\ 0)8_{4,5}$	210 109 231 135.4 ± 2.9
12	$(0\ 2\ 1)5_{3,2} \leftarrow (0\ 0\ 0)4_{3,1}$	210 208 825 509.3 ± 1.9
13	$(0\ 0\ 2)7_{5,3} \leftarrow (0\ 0\ 0)8_{6,2}$	210 238 338 294.5 ± 2.9
14	$(0\ 0\ 2)7_{5,2} \leftarrow (0\ 0\ 0)8_{6,3}$	210 250 167 306.0 ± 2.0
15	$(2\ 0\ 0)6_{2,5} \leftarrow (0\ 0\ 0)7_{1,6}$	210 261 620 255.5 ± 2.4
16	$(2\ 0\ 0)8_{1,8} \leftarrow (0\ 0\ 0)8_{2,7}$	210 373 340 020.8 ± 2.0
17	$(0\ 2\ 1)6_{5,2} \leftarrow (0\ 0\ 0)7_{3,5}$	210 463 636 255.0 ± 1.9
18	$(2\ 0\ 0)7_{4,4} \leftarrow (0\ 0\ 0)7_{5,3}$	210 470 423 741.5 ± 2.5
19	$(1\ 0\ 1)2_{1,2} \leftarrow (0\ 0\ 0)3_{3,1}$	210 514 705 424.9 ± 1.9
20	$(2\ 0\ 0)9_{5,4} \leftarrow (0\ 0\ 0)10_{4,7}$	210 533 593 552.4 ± 2.6
21	$(0\ 0\ 2)6_{1,5} \leftarrow (0\ 0\ 0)7_{4,4}$	210 543 831 004.2 ± 2.1
22	$(0\ 2\ 1)8_{7,2} \leftarrow (0\ 0\ 0)8_{7,1}$	210 623 111 969.9 ± 2.1
23	$(0\ 2\ 1)8_{7,1} \leftarrow (0\ 0\ 0)8_{7,2}$	210 623 149 726.8 ± 2.0
24	$(2\ 0\ 0)6_{4,2} \leftarrow (0\ 0\ 0)6_{5,1}$	210 642 347 124.0 ± 1.9
25	$(2\ 0\ 0)2_{2,1} \leftarrow (0\ 0\ 0)3_{3,0}$	210 751 278 292.3 ± 1.8
26	$(2\ 0\ 0)6_{0,6} \leftarrow (0\ 0\ 0)7_{1,7}$	210 761 361 419.2 ± 2.1
27	$(2\ 0\ 0)4_{1,3} \leftarrow (0\ 0\ 0)5_{2,4}$	210 973 092 183.2 ± 2.1
28	$(0\ 2\ 1)6_{3,3} \leftarrow (0\ 0\ 0)5_{3,2}$	210 984 903 696.3 ± 1.9
29	$(0\ 0\ 2)6_{5,2} \leftarrow (0\ 0\ 0)7_{6,1}$	211 042 347 186.7 ± 3.4
30	$(2\ 0\ 0)9_{7,2} \leftarrow (0\ 0\ 0)10_{6,5}$	211 044 013 161.2 ± 4.9
31	$(0\ 0\ 2)6_{5,1} \leftarrow (0\ 0\ 0)7_{6,2}$	211 044 507 755.4 ± 3.0
32	$(0\ 0\ 2)9_{3,6} \leftarrow (0\ 0\ 0)9_{6,3}$	211 185 551 179.7 ± 7.7
33	$(1\ 0\ 1)5_{2,3} \leftarrow (0\ 0\ 0)5_{4,2}$	211 412 150 018.4 ± 2.0
34	$(2\ 0\ 0)5_{1,5} \leftarrow (0\ 0\ 0)6_{0,6}$	211 474 638 361.0 ± 1.9
35	$(2\ 0\ 0)3_{1,2} \leftarrow (0\ 0\ 0)4_{2,3}$	211 481 121 076.1 ± 2.2
36	$(2\ 0\ 0)8_{6,3} \leftarrow (0\ 0\ 0)9_{5,4}$	211 517 294 984.1 ± 2.2
37	$(2\ 0\ 0)8_{6,2} \leftarrow (0\ 0\ 0)9_{5,5}$	211 601 714 890.4 ± 2.2
38	$(0\ 2\ 1)8_{8,1} \leftarrow (0\ 0\ 0)8_{8,0}$	211 625 155 965.8 ± 12.6
39	$(0\ 2\ 1)8_{8,0} \leftarrow (0\ 0\ 0)8_{8,1}$	211 625 156 251.5 ± 11.3
40	$(1\ 0\ 1)6_{2,4} \leftarrow (0\ 0\ 0)6_{4,3}$	211 757 813 697.5 ± 2.0
41	$(2\ 0\ 0)7_{5,3} \leftarrow (0\ 0\ 0)8_{4,4}$	211 772 255 666.0 ± 1.8
42	$(0\ 2\ 1)6_{4,2} \leftarrow (0\ 0\ 0)5_{4,1}$	211 795 007 175.4 ± 1.8
43	$(2\ 0\ 0)4_{3,1} \leftarrow (0\ 0\ 0)4_{4,0}$	211 869 866 812.5 ± 2.0
44	$(0\ 2\ 1)5_{3,2} \leftarrow (0\ 0\ 0)5_{1,5}$	211 872 275 376.4 ± 2.1
45	$(2\ 0\ 0)6_{0,6} \leftarrow (0\ 0\ 0)6_{1,5}$	212 044 662 857.8 ± 2.0
46	$(2\ 0\ 0)4_{2,3} \leftarrow (0\ 0\ 0)5_{1,4}$	212 061 548 824.1 ± 2.3
47	$(1\ 0\ 1)7_{4,4} \leftarrow (0\ 0\ 0)6_{6,1}$	212 129 230 354.3 ± 2.6
48	$(0\ 2\ 1)3_{3,0} \leftarrow (0\ 0\ 0)2_{1,1}$	212 153 903 036.5 ± 2.7
49	$(2\ 0\ 0)4_{1,4} \leftarrow (0\ 0\ 0)5_{0,5}$	212 167 678 948.1 ± 2.1
50	$(0\ 0\ 2)6_{4,3} \leftarrow (0\ 0\ 0)7_{5,2}$	212 237 422 597.4 ± 2.5
51	$(1\ 0\ 1)7_{4,3} \leftarrow (0\ 0\ 0)6_{6,0}$	212 254 745 824.1 ± 6.1
52	$(1\ 0\ 1)3_{1,3} \leftarrow (0\ 0\ 0)3_{3,0}$	212 326 561 977.8 ± 1.8
53	$(2\ 0\ 0)5_{2,4} \leftarrow (0\ 0\ 0)5_{3,3}$	212 345 214 231.0 ± 2.0

TABLE 1. (*Continued.*)

No.	Assignment	Frequency (kHz)
54	$(2\ 0\ 0)8_{2,6} \leftarrow (0\ 0\ 0)8_{3,5}$	212 396 174 588.1 ± 1.8
55	$(0\ 2\ 1)6_{4,2} \leftarrow (0\ 0\ 0)7_{0,7}$	212 425 021 216.0 ± 1.9
56	$(2\ 0\ 0)1_{1,1} \leftarrow (0\ 0\ 0)2_{2,0}$	212 431 888 691.5 ± 1.8
57	$(2\ 0\ 0)7_{6,2} \leftarrow (0\ 0\ 0)8_{5,3}$	212 457 641 964.8 ± 4.0
58	$(0\ 0\ 2)5_{0,5} \leftarrow (0\ 0\ 0)6_{3,4}$	212 468 032 491.7 ± 1.9
59	$(2\ 0\ 0)7_{6,1} \leftarrow (0\ 0\ 0)8_{5,4}$	212 483 637 001.1 ± 2.5
60	$(0\ 0\ 2)9_{3,6} \leftarrow (0\ 0\ 0)10_{4,7}$	212 522 812 549.7 ± 2.0
61	$(2\ 0\ 0)6_{4,2} \leftarrow (0\ 0\ 0)7_{3,5}$	212 661 534 864.2 ± 5.3
62	$(0\ 2\ 1)6_{3,3} \leftarrow (0\ 0\ 0)6_{1,6}$	212 795 126 999.3 ± 2.9
63	$(2\ 0\ 0)6_{5,2} \leftarrow (0\ 0\ 0)7_{4,3}$	212 822 890 978.6 ± 1.9
64	$(0\ 2\ 1)6_{5,2} \leftarrow (0\ 0\ 0)5_{5,1}$	212 834 466 230.7 ± 2.4
65	$(1\ 0\ 1)9_{4,5} \leftarrow (0\ 0\ 0)10_{2,8}$	212 866 421 839.1 ± 5.7
66	$(2\ 0\ 0)3_{1,3} \leftarrow (0\ 0\ 0)4_{0,4}$	212 872 456 178.3 ± 2.0
67	$(2\ 0\ 0)4_{1,4} \leftarrow (0\ 0\ 0)4_{2,3}$	212 929 950 045.8 ± 2.0
68	$(2\ 0\ 0)6_{1,5} \leftarrow (0\ 0\ 0)6_{2,4}$	213 058 109 278.7 ± 1.9
69	$(0\ 0\ 2)5_{4,1} \leftarrow (0\ 0\ 0)6_{5,2}$	213 059 106 853.4 ± 1.8
70	$(0\ 0\ 2)9_{7,3} \leftarrow (0\ 0\ 0)9_{8,2}$	213 163 968 943.1 ± 6.7
71	$(0\ 0\ 2)9_{7,2} \leftarrow (0\ 0\ 0)9_{8,1}$	213 164 208 347.5 ± 5.8
72	$(2\ 0\ 0)2_{0,2} \leftarrow (0\ 0\ 0)3_{1,3}$	213 210 411 131.7 ± 2.2
73	$(1\ 0\ 1)4_{1,3} \leftarrow (0\ 0\ 0)4_{3,2}$	213 341 078 668.5 ± 1.9
74	$(2\ 0\ 0)3_{1,3} \leftarrow (0\ 0\ 0)3_{2,2}$	213 366 458 394.9 ± 2.2
75	$(0\ 0\ 2)8_{7,2} \leftarrow (0\ 0\ 0)8_{8,1}$	213 391 938 172.9 ± 3.3
76	$(0\ 0\ 2)8_{7,1} \leftarrow (0\ 0\ 0)8_{8,0}$	213 391 975 467.9 ± 2.0
77	$(0\ 2\ 1)6_{4,2} \leftarrow (0\ 0\ 0)6_{2,5}$	213 424 139 718.3 ± 1.9
78	$(2\ 0\ 0)2_{1,2} \leftarrow (0\ 0\ 0)3_{0,3}$	213 607 657 721.6 ± 1.9
79	$(1\ 0\ 1)9_{8,1} \leftarrow (0\ 0\ 0)9_{8,2}$	213 764 920 554.2 ± 2.9
80	$(1\ 0\ 1)9_{8,2} \leftarrow (0\ 0\ 0)9_{8,1}$	213 765 046 786.3 ± 10.5
81	$(0\ 0\ 2)4_{4,1} \leftarrow (0\ 0\ 0)5_{5,0}$	213 838 639 896.6 ± 4.3
82	$(0\ 0\ 2)4_{4,0} \leftarrow (0\ 0\ 0)5_{5,1}$	213 840 105 039.0 ± 4.3
83	$(1\ 0\ 1)8_{8,0} \leftarrow (0\ 0\ 0)8_{8,1}$	213 842 661 994.1 ± 5.4
84	$(1\ 0\ 1)8_{8,1} \leftarrow (0\ 0\ 0)8_{8,0}$	213 842 677 140.0 ± 5.5
85	$(1\ 0\ 1)9_{4,5} \leftarrow (0\ 0\ 0)8_{6,2}$	213 872 692 528.5 ± 6.2
86	$(1\ 0\ 1)3_{0,3} \leftarrow (0\ 0\ 0)4_{0,4}$	214 042 412 142.1 ± 2.7
87	$(2\ 0\ 0)3_{1,2} \leftarrow (0\ 0\ 0)3_{2,1}$	214 113 924 567.5 ± 1.9
88	$(0\ 0\ 2)5_{3,3} \leftarrow (0\ 0\ 0)6_{4,2}$	214 147 221 487.9 ± 2.1
89	$(1\ 0\ 1)2_{2,0} \leftarrow (0\ 0\ 0)3_{2,1}$	214 200 947 005.1 ± 1.7
90	$(1\ 2\ 0)10_{7,4} \leftarrow (0\ 0\ 0)10_{6,5}$	214 260 053 267.7 ± 4.3
91	$(1\ 0\ 1)9_{6,3} \leftarrow (0\ 0\ 0)9_{6,4}$	214 285 337 287.4 ± 5.4
92	$(2\ 0\ 0)1_{1,1} \leftarrow (0\ 0\ 0)2_{0,2}$	214 376 212 856.0 ± 2.0
93	$(0\ 0\ 2)9_{4,5} \leftarrow (0\ 0\ 0)8_{7,2}$	214 446 971 830.5 ± 25.8
94	$(1\ 0\ 1)7_{3,4} \leftarrow (0\ 0\ 0)6_{5,1}$	214 581 817 277.2 ± 2.3
95	$(1\ 0\ 1)7_{3,4} \leftarrow (0\ 0\ 0)8_{1,7}$	214 600 396 009.0 ± 2.4
96	$(2\ 0\ 0)2_{0,2} \leftarrow (0\ 0\ 0)2_{1,1}$	214 612 822 648.1 ± 2.0
97	$(1\ 0\ 1)9_{5,5} \leftarrow (0\ 0\ 0)9_{5,4}$	214 669 009 738.4 ± 2.0
98	$(2\ 0\ 0)9_{6,4} \leftarrow (0\ 0\ 0)8_{7,1}$	214 741 979 846.0 ± 7.5
99	$(0\ 2\ 1)6_{5,2} \leftarrow (0\ 0\ 0)6_{3,3}$	215 084 984 856.9 ± 1.8
100	$(1\ 0\ 1)1_{0,1} \leftarrow (0\ 0\ 0)2_{0,2}$	215 313 738 118.4 ± 2.2
101	$(2\ 0\ 0)5_{3,2} \leftarrow (0\ 0\ 0)4_{4,1}$	215 518 271 848.0 ± 2.5
102	$(2\ 0\ 0)4_{2,3} \leftarrow (0\ 0\ 0)3_{3,0}$	215 540 744 478.2 ± 2.0
103	$(2\ 0\ 0)4_{1,4} \leftarrow (0\ 0\ 0)3_{2,1}$	215 562 753 539.0 ± 2.4
104	$(1\ 0\ 1)7_{4,3} \leftarrow (0\ 0\ 0)7_{4,4}$	215 591 396 440.7 ± 2.0
105	$(1\ 0\ 1)3_{1,3} \leftarrow (0\ 0\ 0)3_{1,2}$	215 607 014 166.6 ± 2.0
106	$(2\ 0\ 0)9_{5,4} \leftarrow (0\ 0\ 0)8_{6,3}$	215 780 605 369.9 ± 2.3
107	$(0\ 0\ 2)4_{2,3} \leftarrow (0\ 0\ 0)5_{3,2}$	215 812 069 399.3 ± 2.0

TABLE 1. (*Continued.*)

No.	Assignment	Frequency (kHz)
108	$(0\ 0\ 2)7_{5,3} \leftarrow (0\ 0\ 0)7_{6,2}$	216 093 103 792.3 ± 2.6
109	$(0\ 0\ 2)7_{5,2} \leftarrow (0\ 0\ 0)7_{6,1}$	216 103 706 730.5 ± 5.9
110	$(1\ 0\ 1)2_{1,2} \leftarrow (0\ 0\ 0)2_{1,1}$	216 129 993 563.2 ± 2.2
111	$(0\ 0\ 2)6_{5,2} \leftarrow (0\ 0\ 0)6_{6,1}$	216 168 223 250.8 ± 2.5
112	$(0\ 0\ 2)6_{5,1} \leftarrow (0\ 0\ 0)6_{6,0}$	216 170 204 632.1 ± 2.3
113	$(1\ 0\ 1)5_{2,3} \leftarrow (0\ 0\ 0)6_{0,6}$	216 199 773 829.6 ± 2.3
114	$(2\ 0\ 0)3_{1,2} \leftarrow (0\ 0\ 0)3_{0,3}$	216 346 256 445.2 ± 1.9
115	$(2\ 0\ 0)2_{0,2} \leftarrow (0\ 0\ 0)1_{1,1}$	216 352 817 189.0 ± 1.8
116	$(2\ 0\ 0)3_{1,2} \leftarrow (0\ 0\ 0)2_{2,1}$	216 432 023 528.1 ± 1.8
117	$(1\ 0\ 1)2_{2,0} \leftarrow (0\ 0\ 0)3_{0,3}$	216 433 278 881.6 ± 1.8
118	$(2\ 0\ 0)1_{1,1} \leftarrow (0\ 0\ 0)0_{0,0}$	216 472 584 311.6 ± 1.8
119	$(1\ 2\ 0)8_{8,0} \leftarrow (0\ 0\ 0)8_{7,1}$	216 483 694 353.7 ± 9.0
120	$(1\ 2\ 0)8_{8,1} \leftarrow (0\ 0\ 0)8_{7,2}$	216 483 717 383.2 ± 6.7
121	$(0\ 2\ 1)8_{7,2} \leftarrow (0\ 0\ 0)7_{7,1}$	216 489 812 790.6 ± 3.8
122	$(0\ 2\ 1)8_{7,1} \leftarrow (0\ 0\ 0)7_{7,0}$	216 489 825 683.5 ± 2.4
123	$(0\ 2\ 1)6_{4,2} \leftarrow (0\ 0\ 0)5_{2,3}$	216 580 721 741.8 ± 2.2
124	$(1\ 0\ 1)3_{0,3} \leftarrow (0\ 0\ 0)2_{2,0}$	216 634 144 652.6 ± 1.8
125	$(0\ 0\ 2)7_{1,7} \leftarrow (0\ 0\ 0)6_{4,2}$	216 757 805 909.1 ± 2.0
126	$(1\ 0\ 1)9_{3,6} \leftarrow (0\ 0\ 0)8_{5,3}$	216 799 357 582.5 ± 3.8
127	$(2\ 0\ 0)2_{2,1} \leftarrow (0\ 0\ 0)2_{1,2}$	216 846 609 141.3 ± 1.8
128	$(0\ 0\ 2)9_{7,2} \leftarrow (0\ 0\ 0)10_{6,5}$	216 968 496 740.6 ± 14.5
129	$(2\ 0\ 0)2_{1,2} \leftarrow (0\ 0\ 0)1_{0,1}$	216 982 773 517.9 ± 2.1
130	$(0\ 0\ 2)6_{1,5} \leftarrow (0\ 0\ 0)7_{2,6}$	216 998 301 710.3 ± 5.4
131	$(2\ 0\ 0)6_{5,2} \leftarrow (0\ 0\ 0)7_{2,5}$	217 177 283 403.9 ± 2.1
132	$(2\ 0\ 0)8_{6,3} \leftarrow (0\ 0\ 0)9_{3,6}$	217 177 808 391.7 ± 5.5
133	$(2\ 0\ 0)4_{1,3} \leftarrow (0\ 0\ 0)3_{2,2}$	217 251 114 072.7 ± 2.2
134	$(2\ 0\ 0)4_{2,3} \leftarrow (0\ 0\ 0)4_{1,4}$	217 293 885 932.1 ± 1.9
135	$(1\ 0\ 1)5_{4,2} \leftarrow (0\ 0\ 0)6_{2,5}$	217 331 676 827.7 ± 1.8
136	$(0\ 0\ 2)6_{4,3} \leftarrow (0\ 0\ 0)6_{5,2}$	217 367 677 127.3 ± 1.8
137	$(2\ 0\ 0)3_{1,3} \leftarrow (0\ 0\ 0)2_{0,2}$	217 408 512 852.7 ± 2.1
138	$(1\ 0\ 1)1_{0,1} \leftarrow (0\ 0\ 0)0_{0,0}$	217 410 109 567.6 ± 1.7
139	$(0\ 0\ 2)5_{4,1} \leftarrow (0\ 0\ 0)5_{5,0}$	217 447 865 443.1 ± 2.1
140	$(1\ 0\ 1)9_{8,2} \leftarrow (0\ 0\ 0)10_{6,5}$	217 569 335 181.0 ± 25.3
141	$(2\ 0\ 0)5_{2,4} \leftarrow (0\ 0\ 0)5_{1,5}$	217 602 988 556.8 ± 1.8
142	$(2\ 0\ 0)7_{4,4} \leftarrow (0\ 0\ 0)7_{3,5}$	217 612 335 109.7 ± 1.9
143	$(0\ 0\ 2)9_{4,5} \leftarrow (0\ 0\ 0)9_{5,4}$	217 626 736 744.6 ± 2.2
144	$(1\ 0\ 1)6_{2,4} \leftarrow (0\ 0\ 0)6_{2,5}$	217 771 112 596.2 ± 2.3
145	$(0\ 0\ 2)8_{7,1} \leftarrow (0\ 0\ 0)9_{6,4}$	217 886 018 263.8 ± 25.3
146	$(2\ 0\ 0)7_{5,3} \leftarrow (0\ 0\ 0)7_{4,4}$	217 904 310 316.5 ± 1.8
147	$(2\ 0\ 0)6_{2,5} \leftarrow (0\ 0\ 0)6_{1,6}$	217 946 740 820.4 ± 1.8
148	$(2\ 0\ 0)2_{2,1} \leftarrow (0\ 0\ 0)1_{1,0}$	217 954 798 734.0 ± 2.2
149	$(2\ 0\ 0)9_{6,4} \leftarrow (0\ 0\ 0)9_{5,5}$	217 999 528 718.1 ± 3.1
150	$(1\ 0\ 1)4_{1,3} \leftarrow (0\ 0\ 0)4_{1,4}$	218 001 743 321.6 ± 2.4
151	$(2\ 0\ 0)6_{5,2} \leftarrow (0\ 0\ 0)6_{4,3}$	218 059 270 648.7 ± 1.8
152	$(2\ 0\ 0)10_{7,4} \leftarrow (0\ 0\ 0)10_{6,5}$	218 150 542 878.7 ± 6.1
153	$(2\ 0\ 0)8_{6,2} \leftarrow (0\ 0\ 0)8_{5,3}$	218 161 537 779.0 ± 2.4
154	$(2\ 0\ 0)5_{1,5} \leftarrow (0\ 0\ 0)4_{0,4}$	218 178 362 696.5 ± 1.9
155	$(2\ 0\ 0)8_{6,3} \leftarrow (0\ 0\ 0)8_{5,4}$	218 179 986 634.9 ± 1.9
156	$(2\ 0\ 0)7_{6,1} \leftarrow (0\ 0\ 0)7_{5,2}$	218 334 548 220.7 ± 2.0
157	$(2\ 0\ 0)7_{6,2} \leftarrow (0\ 0\ 0)7_{5,3}$	218 340 043 754.4 ± 2.0
158	$(2\ 0\ 0)9_{7,2} \leftarrow (0\ 0\ 0)9_{6,3}$	218 340 933 409.3 ± 2.8
159	$(2\ 0\ 0)9_{7,3} \leftarrow (0\ 0\ 0)9_{6,4}$	218 345 299 533.4 ± 3.4
160	$(2\ 0\ 0)3_{2,2} \leftarrow (0\ 0\ 0)2_{1,1}$	218 439 924 827.2 ± 1.9
161	$(0\ 0\ 2)5_{0,5} \leftarrow (0\ 0\ 0)6_{1,6}$	218 464 971 503.2 ± 2.1
162	$(2\ 0\ 0)6_{0,6} \leftarrow (0\ 0\ 0)5_{1,5}$	218 519 112 560.5 ± 1.9
163	$(0\ 0\ 2)5_{3,3} \leftarrow (0\ 0\ 0)5_{4,2}$	218 573 455 208.2 ± 2.1
164	$(1\ 0\ 1)3_{0,3} \leftarrow (0\ 0\ 0)2_{0,2}$	218 578 468 816.8 ± 2.0
165	$(0\ 0\ 2)6_{4,3} \leftarrow (0\ 0\ 0)7_{3,4}$	218 582 638 989.0 ± 2.3
166	$(0\ 2\ 1)6_{5,2} \leftarrow (0\ 0\ 0)6_{1,5}$	218 605 445 288.7 ± 2.0
167	$(0\ 0\ 2)4_{3,2} \leftarrow (0\ 0\ 0)4_{4,1}$	218 657 009 780.6 ± 4.4
168	$(2\ 0\ 0)6_{1,5} \leftarrow (0\ 0\ 0)5_{2,4}$	218 666 316 036.3 ± 2.2
169	$(1\ 2\ 0)10_{5,6} \leftarrow (0\ 0\ 0)10_{2,9}$	218 682 073 260.7 ± 4.3
170	$(0\ 0\ 2)4_{3,1} \leftarrow (0\ 0\ 0)4_{4,0}$	218 712 072 101.4 ± 4.3
171	$(2\ 0\ 0)4_{2,3} \leftarrow (0\ 0\ 0)3_{1,2}$	218 821 196 666.6 ± 1.9
172	$(0\ 2\ 1)7_{5,3} \leftarrow (0\ 0\ 0)7_{1,6}$	218 876 570 693.2 ± 2.2
173	$(2\ 0\ 0)7_{0,7} \leftarrow (0\ 0\ 0)6_{1,6}$	218 924 924 113.5 ± 2.1
174	$(2\ 0\ 0)7_{1,7} \leftarrow (0\ 0\ 0)6_{0,6}$	218 944 686 727.2 ± 2.2
175	$(0\ 2\ 1)8_{3,6} \leftarrow (0\ 0\ 0)7_{1,7}$	218 953 589 662.3 ± 4.2
176	$(0\ 0\ 2)4_{2,3} \leftarrow (0\ 0\ 0)5_{1,4}$	219 030 888 618.5 ± 2.2
177	$(2\ 0\ 0)5_{2,4} \leftarrow (0\ 0\ 0)4_{1,3}$	219 114 318 272.8 ± 1.8
178	$(1\ 0\ 1)10_{4,7} \leftarrow (0\ 0\ 0)10_{2,8}$	219 116 362 450.6 ± 2.9
179	$(2\ 0\ 0)8_{0,8} \leftarrow (0\ 0\ 0)7_{1,7}$	219 303 346 196.8 ± 1.6
180	$(2\ 0\ 0)8_{1,8} \leftarrow (0\ 0\ 0)7_{0,7}$	219 311 239 691.7 ± 1.8
181	$(1\ 0\ 1)5_{4,2} \leftarrow (0\ 0\ 0)4_{4,1}$	219 364 489 739.6 ± 2.2
182	$(2\ 0\ 0)8_{2,6} \leftarrow (0\ 0\ 0)7_{3,5}$	219 428 314 316.7 ± 2.0
183	$(2\ 0\ 0)6_{4,2} \leftarrow (0\ 0\ 0)7_{1,7}$	219 520 042 451.7 ± 4.9
184	$(1\ 0\ 1)7_{4,4} \leftarrow (0\ 0\ 0)7_{2,5}$	219 706 219 845.0 ± 1.8
185	$(0\ 0\ 2)9_{7,3} \leftarrow (0\ 0\ 0)8_{8,0}$	219 775 912 292.8 ± 4.5
186	$(0\ 0\ 2)9_{7,2} \leftarrow (0\ 0\ 0)8_{8,1}$	219 776 155 143.7 ± 4.9
187	$(1\ 0\ 1)2_{2,0} \leftarrow (0\ 0\ 0)1_{0,1}$	219 808 394 678.7 ± 2.0
188	$(1\ 0\ 1)9_{6,3} \leftarrow (0\ 0\ 0)10_{2,8}$	219 857 498 428.2 ± 18.3
189	$(1\ 0\ 1)8_{7,1} \leftarrow (0\ 0\ 0)7_{7,0}$	219 863 960 903.2 ± 2.6
190	$(1\ 0\ 1)8_{7,2} \leftarrow (0\ 0\ 0)7_{7,1}$	219 864 205 780.9 ± 2.9
191	$(0\ 0\ 2)6_{1,5} \leftarrow (0\ 0\ 0)5_{4,2}$	220 057 792 912.1 ± 2.5
192	$(0\ 0\ 2)5_{4,1} \leftarrow (0\ 0\ 0)6_{3,4}$	220 095 044 911.2 ± 1.9
193	$(1\ 2\ 0)8_{5,4} \leftarrow (0\ 0\ 0)7_{2,5}$	220 187 752 450.6 ± 2.0
194	$(2\ 0\ 0)4_{3,1} \leftarrow (0\ 0\ 0)3_{2,2}$	220 201 599 204.0 ± 2.0
195	$(0\ 2\ 1)6_{4,2} \leftarrow (0\ 0\ 0)5_{0,5}$	220 211 562 785.8 ± 1.8

[a]The assignments given follow the notation of Fig. 4. The uncertainties behind the ± signs represent 68% confidence level. Note that three of the listed transitions were determined to be 214 200 946 980(30) kHz $[(1\ 0\ 1)2_{2,0} \leftarrow (0\ 0\ 0)3_{2,1}]$, 215 607 014 210(30) kHz $[(1\ 0\ 1)3_{1,3} \leftarrow (0\ 0\ 0)3_{1,2}]$, and 216 129 993 490(30) kHz $[(1\ 0\ 1)2_{1,2} \leftarrow (0\ 0\ 0)2_{1,1}]$ by Gambetta *et al.*,[37] showing deviations of 25, 43, and 73 kHz from the NICE-OHMS frequencies, accurate to about 2 kHz, respectively.

candidates for the virtual transitions as their energy differences, here called 0/1 splittings, can be obtained with high accuracy via state-of-the-art variational nuclear-motion computations.[57] These accurate quantum-chemical computations were executed here with the latest version[58] of the fourth-age[57] GENIUSH (**GE**neral rovibrational code with **N**umerical, **I**nternal-coordinate, **U**ser-**S**pecified **H**amiltonians) code.[59,60]

During the quantum-chemical computations, enlarged vibrational basis sets were utilized, involving multiple potential energy surfaces (PESs) of spectroscopic quality. Several outstanding PESs have been reported in the literature for $H_2^{16}O$ and $H_2^{18}O$,[61–64] which can be employed to deduce accurate 0/1

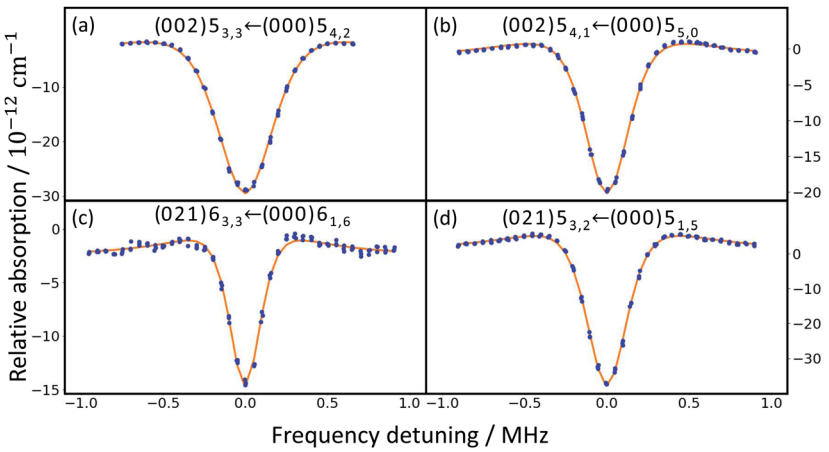

FIG. 6. Lamb-dip spectra of four typical $H_2^{18}O$ transitions recorded with the NICE-OHMS setup. On the left and right panels, *para*- and *ortho*-$H_2^{18}O$ transitions are depicted, respectively. The Lamb dips are plotted along the same (relative) frequency axis, and they exhibit varying degree of power broadening. The vertical axis refers to relative absorption strengths for the Lamb dips.

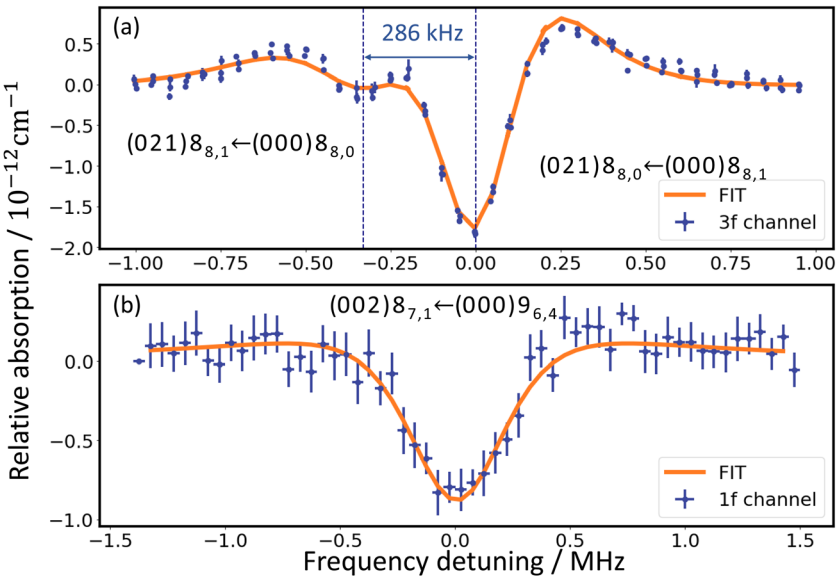

FIG. 7. Recordings of unusual features in the spectra of $H_2^{18}O$. Panel (a) shows the Lamb-dip spectrum of the (0 2 1)$8_{8,0/1}$ ← (0 0 0)$8_{8,1/0}$ doublet measured by the 3*f* demodulation technique in saturation by the power circulating on the sideband frequency. Panel (b) exhibits the Lamb-dip profile of the weakest ($S = 1.4 \times 10^{-27}$ cm molecule^{-1} and $A_E = 1.5 \times 10^{-3}$ s^{-1}) line probed during the experimental campaign, (0 0 2)$8_{7,1}$ ← (0 0 0)$9_{6,4}$, averaging over 20 scans.

splittings. As the computational details are quite similar to those presented in Supplementary Note 4 of Ref. 48, only the most important aspects are emphasized here. Above all, in spite of the fact that absolute energies cannot be determined with an accuracy comparable to (ultra)high-precision experiments, the 0/1 splittings can have ultrasmall uncertainties. The reason is that energy shifts resulting from deficiencies of the PES are almost fully compensated when differences between rovibrational energies of highly similar, nearby states are formed. In addition, errors arising from the incompleteness of the vibrational basis set are also wiped out this way (the rotational basis is complete). As a consequence, the 0/1 splittings are more or less independent of the PESs and the basis sets used for their computation.

Besides the 0/1 splittings, the energy differences of other close *ortho*/*para* state pairs, differing only in their K_a or K_c numbers, can also be derived with high accuracy. Similarly precise predictions can be given for the relative positions, both their signs and absolute values, of nearby ($U_1 \leftarrow L_1$, $U_2 \leftarrow L_2$) transition doublets, showing roughly 1:3 intensity ratios, where U_1/U_2 and L_1/L_2 are *ortho*/*para* or *para*/*ortho* state pairs. These relative positions can be determined from a properly signed sum of the underlying *ortho*/*para* energy splittings.

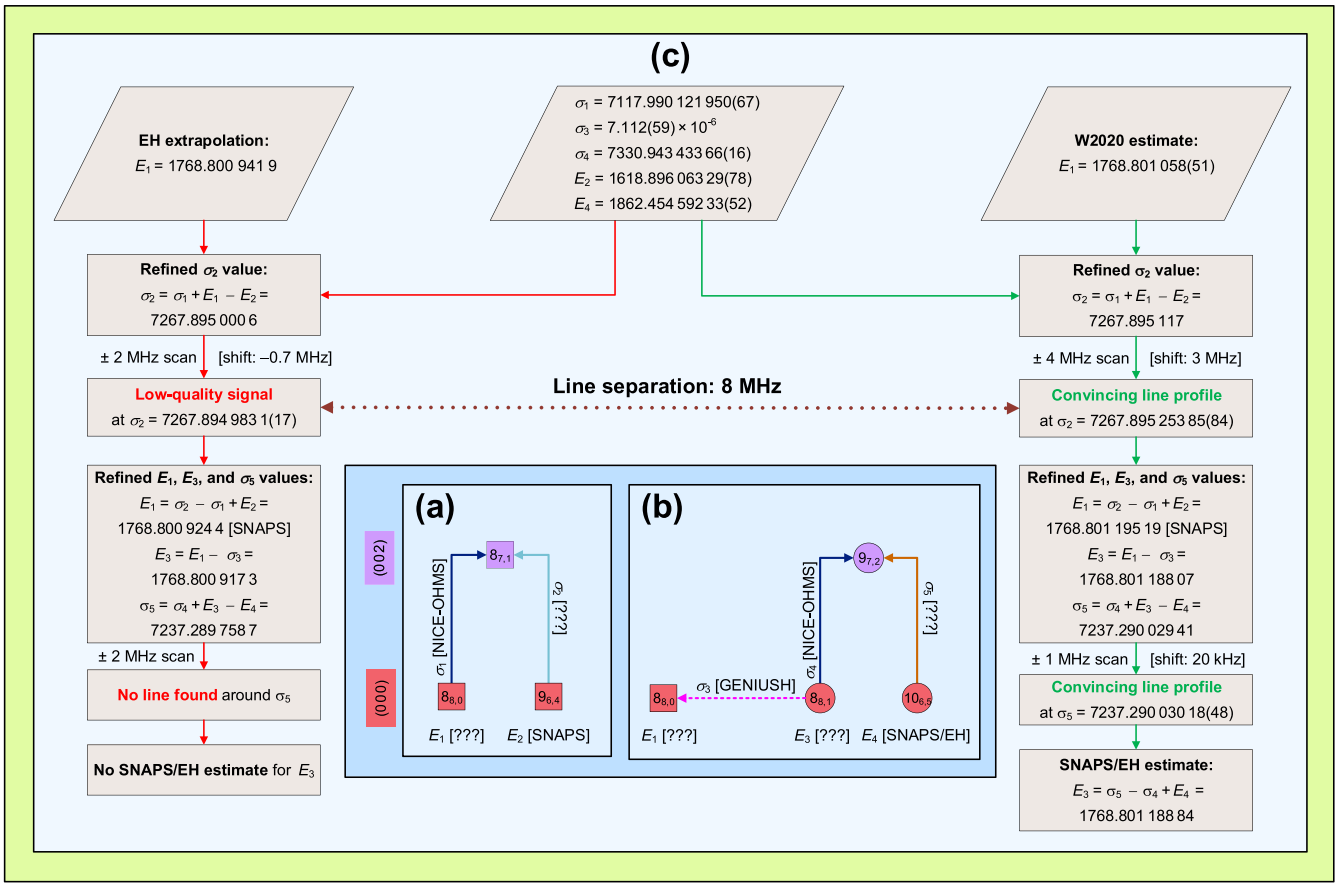

FIG. 8. Story of the detection of the two weak lines necessary for the determination of the (0 0 0)$8_{8,0/1}$ states. Panels (a) and (b) indicate the two weak transitions (in light blue and brown) selected for measurement and define the parameters of this figure with their origin (NICE-OHMS observation, SNAPS-based estimate, combined SNAPS/EH prediction, or GENIUSH computation). The SNAPS/EH combination means here that the relative SNAPS energy values are converted to absolute energies by including the (0 0 0)$1_{0,1}$ energy deduced from an EH model (see also Sec. 3.6). The specification of the energy levels is the same as in Figs. 4 and 5. If the σ_3 (virtual) line is not considered, then these two panels correspond to Λ-correction schemes. Panel (c) presents two routes for the observation of the two weak lines (where no units are given, the data are in cm^{-1}). The left route, represented with red arrows, relies on the energy value of the (0 0 0)$8_{8,0}$ state extrapolated from a preliminary EH fit. This route provided a low-quality Lamb-dip profile for the light blue transition around the refined (initial) σ_2 value in a range of ±2 MHz, shifted by –0.7 MHz. Based on the center of this scattered profile, no signal could be found for the brown line by scanning a region of ±2 MHz around the adjusted (initial) σ_5 wavenumber. Therefore, the right route, illustrated with green arrows, was tried, where the W2020 energy of (0 0 0)$8_{8,0}$, having an uncertainty of ~1.5 MHz, was adopted to give a refined σ_2 line position. From this empirical energy, a well-behaved Lamb-dip curve [see Fig. 7(b)] could be recorded whose position is translated by 3 MHz from the W2020-based prediction for σ_2. The newly probed line is separated by 8 MHz from that resolved on the left route, which must be a ghost transition produced by the optical system of NICE-OHMS. Then, drawing on the NICE-OHMS value of σ_2 and σ_3 splittings (see Sec. 3.5), an accurate estimate could be derived for σ_5, from which a similarly correct line profile was observed for the brown transition with a shift of just 20 kHz. With the aid of the experimental σ_5 position, the SNAPS/EH prediction for (0 0 0)$8_{8,1}$ could be derived.

3. Results and Discussion

3.1. Ultraprecise NICE-OHMS spectra

Lamb dips of 195 rovibrational transitions, involving six vibrational bands [(0 0 0), (1 2 0), (0 2 1), (2 0 0), (1 0 1), and (0 0 2)] and characterized with $J \leq 11$, were recorded. Due to the careful (SNAPS) design of the NICE-OHMS measurements, the ultraprecise lines of both *ortho*- and *para*-$H_2^{18}O$ are internally connected, allowing the transfer of the observational accuracy to that of the derived relative energies. Typical Lamb-dip spectra of the observed transitions are seen in Fig. 6.

As one of the most important experimental results of this work, nine transition doublets separated by less than 300 MHz were observed. Resolution of these closely spaced lines is far from trivial in Doppler-limited spectroscopy, if feasible at all. Thus, it is not surprising that while these nine doublets were studied, they could not be resolved in Refs. 65–68, which reported a single wavenumber for each of these pairs. In the NICE-OHMS spectra, the lines of these doublets, with a separation greater than 300 kHz, are well isolated, yielding accurate individual frequencies for the underlying transitions.

It is emphasized that these small doublet separations derived from NICE-OHMS spectra can be reproduced well by quantum-chemical computations having a relative uncertainty of 1%–5%. For example, the separation of (1 0 1)$9_{8,2/1} \leftarrow$ (0 0 0)$9_{8,1/2}$ is measured as 126.232 1(109) MHz by NICE-OHMS, which agrees well with the

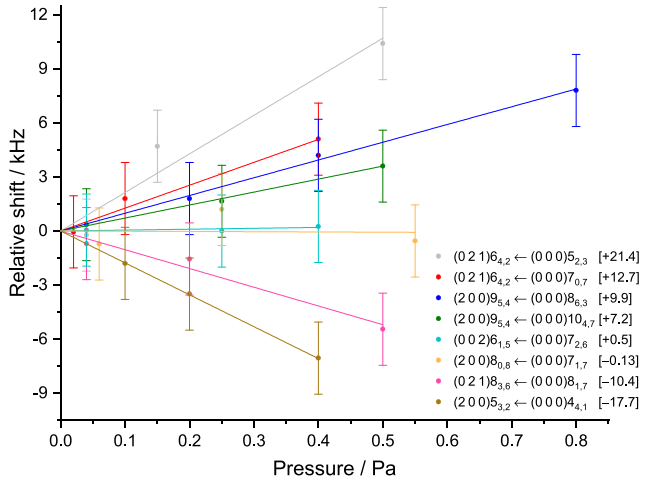

FIG. 9. Pressure shifts of the Lamb-dip centers for a number of selected transitions in $H_2{}^{18}O$. The shifts are related to the line frequencies in vacuum. The rovibrational assignments and the pressure-shift coefficients (slopes, inside the brackets, given in kHz Pa^{-1}) are provided for each line in the legend to the figure.

quantum-chemical prediction of 128.1(24) MHz, obtained as part of this study (see Secs. 2.3 and 3.5). Likewise, the NICE-OHMS separation of the (0 2 1)$8_{8,0/1}$ ← (0 0 0)$8_{8,1/0}$ doublet, 286(17) kHz, agrees with its quantum-chemical counterpart, 306(13) kHz.

The last extremely close-lying doublet, with a separation at the border of our resolvability limit (300 kHz), could still be resolved, at least partially, by exploiting some special features of the NICE-OHMS technique: here, we relied on 3*f*-demodulation with the lock-in detector and recording of the Lamb-dip features via saturation by the sideband power shifted by one FSR. The spectrum of this doublet is presented in Fig. 7(a). The optical methods applied will be discussed in a future publication.

The lines probed during the measurement campaign for *para*- and *ortho*-$H_2{}^{18}O$ are presented in Figs. 4 and 5, respectively. The measurements were designed to cover all the (0 0 0)J_{K_a,K_c} states up to $J = 8$; thus, these transitions are very different both in their S and A_E values. Lines incident to low-K_a states were straightforwardly detectable due to their ideal strength ($A_E = 10^{-3}$–1 s^{-1} and $S = 10^{-25}$–10^{-21} cm molecule^{-1}), while those linking $K_a > J/2$ levels were considerably weaker ($S < 1 \times 10^{-26}$ cm molecule^{-1}), making their experimental study challenging. The improved accuracy of the initial positions achieved via the Λ-correction scheme (see Sec. 2.2) reduced significantly the technical difficulties, but observation of the weakest line profile [see Fig. 7(b)] still remained difficult. It was a complicated task to build suitable paths linking the (0 0 0)$8_{8,0/1}$ energy levels to the lowest-energy *para*/*ortho* states. The first (unsuccessful) and the second (successful) routes to find an experimental realization for these paths is outlined in Fig. 8.

Another issue beyond line strength is that transitions located in the close vicinity of a particular target line may disturb its observation. These disturbing lines, corresponding to $H_2{}^{18}O$, $H_2{}^{16}O$, and even $HD^{18}O$, can distort and often conceal the target transition completely. As an empirical rule, candidate lines adjacent to too strong ($S > 1 \times 10^{-23}$ cm molecule^{-1}) $H_2{}^{16}O$ lines at a distance smaller than 350 MHz could not be properly resolved due to spectral overlaps. Thus, such candidates were mostly not considered during the SNAPS analysis.

In the cases when the adjacent lines have almost identical S and A_E values, one cannot fully decide which water isotopologue is interrogated by the spectroscopy laser. For example, when the (2 0 0)$6_{4,2}$ ← (0 0 0)$6_{5,1}$ transition of $H_2{}^{18}O$ was targeted, its neighboring $H_2{}^{16}O$ line, (0 2 1)$6_{2,5}$ ← (0 0 0)$5_{2,4}$, separated by just 10 MHz, was accidentally measured (these close-lying lines would be unresolvable under Doppler-broadened conditions, distorting the effective position of the unresolved line pair). A similar "mistake" was made during the planned observation of the (2 0 0)$9_{7,2}$ ← (0 0 0)$9_{6,3}$ transition of $H_2{}^{18}O$: in this case, the (0 0 2)$4_{3,1}$ ← (0 0 0)$4_{2,2}$ line of $HD^{18}O$, located 39 MHz away from the $H_2{}^{18}O$ line, was probed. These issues were discovered when the discrepancies of the newly formed cycles were analyzed as part of the SNAPS scheme, and the EH fit was performed for the lower-state energy differences of the Λ shapes (Fig. 2) composed of NICE-OHMS transitions. The six-membered cycle that helped reveal the inconsistency in the first example given can be inspected in Fig. 3(d).

3.2. Uncertainty quantification

The uncertainties of the line positions listed in Table 1 depend on several experimental factors. In this study, the following decomposition is used to estimate the frequency uncertainty (δ):

$$\delta = \sqrt{\delta_{stat}^2 + \delta_{day}^2 + \delta_{cal}^2 + \delta_{pow}^2 + \delta_{pres}^2},$$

where the meaning of the individual terms is explained below.

The statistical uncertainty, δ_{stat}, gauges the reproducibility of the NICE-OHMS frequencies. For transitions with ideal strength, δ_{stat} is approximated as the standard deviation of the line centers obtained from 3 to 4 scans (requiring about 10 min for each scan). For extremely weak ($S < 10^{-26}$ cm molecule^{-1}) lines, δ_{stat} is estimated individually from their data-averaged spectra overlaid by multiple scans (the locking of the diode laser to the OFC laser enabled merging multiple recordings without causing drifts on the frequency scale). Due to the high sensitivity of the NICE-OHMS spectrometer, the very strong ($A_E > 1$ s^{-1}) transitions with low J values may be affected by power broadening, inducing somewhat larger δ_{stat} values in certain cases. Similarly, in our pressure range (0.03–1.0 Pa), pressure broadening effected by molecular collisions also leads to a slight increase in δ_{stat}, at least for a few lines.

The day-to-day uncertainty, δ_{day}, is connected to δ_{stat}, characterizing the *long-term* reproducibility of the line frequencies and the stability of the NICE-OHMS setup. The spectra of some transitions were repeatedly recorded on two to three different days, yielding an average deviation of 1.5 kHz for these lines. This average deviation is assigned to δ_{day}, as a conservative estimate, for each transition observed with NICE-OHMS.

If a target transition could not be properly detected from the main signal (mostly due to disturbing lines within the scanning range), then this candidate is extracted from a sideband signal, which can be calibrated with an accuracy of only 5–10 kHz. Therefore, an additional calibration uncertainty, δ_{cal}, is included in the uncertainty budget, setting $\delta_{cal} = 5$ kHz or $\delta_{cal} = 10$ kHz for sideband-based transitions and $\delta_{cal} = 0$ for the other lines.

TABLE 2. SNAPS-based relative energies, in cm^{-1}, for states within the (0 0 0) vibrational band of $H_2^{18}O$[a]

Assignment	Relative Energy (cm^{-1})	Assignment	Relative Energy (cm^{-1})
	para-$H_2^{18}O$		*ortho*-$H_2^{18}O$
$(0\ 0\ 0)0_{0,0}$	0.0	$(0\ 0\ 0)1_{0,1}$	0.0
$(0\ 0\ 0)1_{1,1}$	36.748 658 33(18)	$(0\ 0\ 0)1_{1,0}$	18.268 520 34(21)
$(0\ 0\ 0)2_{0,2}$	69.927 424 779(90)	$(0\ 0\ 0)2_{1,2}$	55.233 746 22(20)
$(0\ 0\ 0)2_{1,1}$	94.788 628 80(19)	$(0\ 0\ 0)2_{2,1}$	109.720 862 72(12)
$(0\ 0\ 0)2_{2,0}$	134.783 097 849(85)	$(0\ 0\ 0)3_{0,3}$	112.581 744 705(90)
$(0\ 0\ 0)3_{1,3}$	141.568 041 65(16)	$(0\ 0\ 0)3_{1,2}$	149.127 991 58(18)
$(0\ 0\ 0)3_{2,2}$	204.755 848 57(14)	$(0\ 0\ 0)3_{2,1}$	187.044 320 962(88)
$(0\ 0\ 0)3_{3,1}$	282.094 479 51(21)	$(0\ 0\ 0)3_{3,0}$	258.552 098 18(18)
$(0\ 0\ 0)4_{0,4}$	221.233 988 82(13)	$(0\ 0\ 0)4_{1,4}$	200.073 593 90(16)
$(0\ 0\ 0)4_{1,3}$	274.803 169 05(17)	$(0\ 0\ 0)4_{2,3}$	274.865 192 41(13)
$(0\ 0\ 0)4_{2,2}$	314.459 423 65(13)	$(0\ 0\ 0)4_{3,2}$	355.536 632 70(19)
$(0\ 0\ 0)4_{3,1}$	380.702 416 96(17)	$(0\ 0\ 0)4_{4,1}$	458.888 542 82(19)
$(0\ 0\ 0)4_{4,0}$	482.672 526 23(17)	$(0\ 0\ 0)5_{0,5}$	300.291 819 37(14)
$(0\ 0\ 0)5_{1,5}$	325.215 701 98(15)	$(0\ 0\ 0)5_{1,4}$	374.605 573 22(19)
$(0\ 0\ 0)5_{2,4}$	414.168 117 69(17)	$(0\ 0\ 0)5_{2,3}$	421.403 640 13(17)
$(0\ 0\ 0)5_{3,3}$	500.596 175 55(17)	$(0\ 0\ 0)5_{3,2}$	481.973 825 27(21)
$(0\ 0\ 0)5_{4,2}$	604.544 103 53(19)	$(0\ 0\ 0)5_{4,1}$	581.037 895 05(16)
$(0\ 0\ 0)5_{5,1}$	733.679 238 47(20)	$(0\ 0\ 0)5_{5,0}$	709.928 031 39(28)
$(0\ 0\ 0)6_{0,6}$	444.846 163 06(16)	$(0\ 0\ 0)6_{1,6}$	421.591 275 45(24)
$(0\ 0\ 0)6_{1,5}$	541.180 097 68(17)	$(0\ 0\ 0)6_{2,5}$	526.695 882 79(16)
$(0\ 0\ 0)6_{2,4}$	601.237 758 97(20)	$(0\ 0\ 0)6_{3,4}$	621.627 628 98(26)
$(0\ 0\ 0)6_{3,3}$	658.610 017 54(19)	$(0\ 0\ 0)6_{4,3}$	727.277 943 42(19)
$(0\ 0\ 0)6_{4,2}$	752.187 368 14(21)	$(0\ 0\ 0)6_{5,2}$	856.321 260 19(27)
$(0\ 0\ 0)6_{5,1}$	880.114 466 94(25)	$(0\ 0\ 0)6_{6,1}$	1 009.439 035 53(24)
$(0\ 0\ 0)6_{6,0}$	1 033.194 397 48(31)	$(0\ 0\ 0)7_{0,7}$	560.022 888 71(16)
$(0\ 0\ 0)7_{1,7}$	583.986 426 00(17)	$(0\ 0\ 0)7_{1,6}$	677.939 304 22(26)
$(0\ 0\ 0)7_{2,6}$	706.597 744 73(19)	$(0\ 0\ 0)7_{2,5}$	756.697 871 15(21)
$(0\ 0\ 0)7_{3,5}$	812.761 614 04(20)	$(0\ 0\ 0)7_{3,4}$	815.794 494 78(29)
$(0\ 0\ 0)7_{4,4}$	921.895 713 09(22)	$(0\ 0\ 0)7_{4,3}$	901.944 768 10(21)
$(0\ 0\ 0)7_{5,3}$	1 050.990 134 39(22)	$(0\ 0\ 0)7_{5,2}$	1 027.448 131 23(29)
$(0\ 0\ 0)7_{6,2}$	1 204.169 241 57(33)	$(0\ 0\ 0)7_{6,1}$	1 180.419 856 67(28)
$(0\ 0\ 0)7_{7,1}$	1 378.986 135 19(42)	$(0\ 0\ 0)7_{7,0}$	1 355.231 288 07(93)
$(0\ 0\ 0)8_{0,8}$	740.912 244 22(19)	$(0\ 0\ 0)8_{1,8}$	717.243 671 54(26)
$(0\ 0\ 0)8_{1,7}$	879.494 747 17(23)	$(0\ 0\ 0)8_{2,7}$	858.159 130 38(19)
$(0\ 0\ 0)8_{2,6}$	980.222 237 92(25)	$(0\ 0\ 0)8_{3,6}$	977.950 777 34(28)
$(0\ 0\ 0)8_{3,5}$	1 047.328 546 62(22)	$(0\ 0\ 0)8_{4,5}$	1 092.881 155 49(24)
$(0\ 0\ 0)8_{4,4}$	1 126.439 039 21(23)	$(0\ 0\ 0)8_{5,4}$	1 222.613 521 94(31)
$(0\ 0\ 0)8_{5,3}$	1 247.205 937 44(27)	$(0\ 0\ 0)8_{6,3}$	1 375.672 914 85(35)
$(0\ 0\ 0)8_{6,2}$	1 399.463 197 16(36)	$(0\ 0\ 0)8_{7,2}$	1 550.922 533 80(92)
$(0\ 0\ 0)8_{7,1}$	1 574.678 210 30(40)	$(0\ 0\ 0)8_{8,1}$	1 745.046 284 23(71)
$(0\ 0\ 0)8_{8,0}$	1 768.801 195 2(12)	$(0\ 0\ 0)9_{3,6}$	1 256.042 589 83(37)
$(0\ 0\ 0)9_{5,5}$	1 466.018 076 09(29)	$(0\ 0\ 0)9_{5,4}$	1 444.856 993 15(33)
$(0\ 0\ 0)9_{6,4}$	1 618.896 063 29(78)	$(0\ 0\ 0)9_{6,3}$	1 595.300 627 69(45)
$(0\ 0\ 0)9_{8,2}$	1 989.351 885 3(12)	$(0\ 0\ 0)9_{8,1}$	1 965.597 089 29(71)
$(0\ 0\ 0)10_{2,8}$	1 433.028 774 36(45)	$(0\ 0\ 0)10_{2,9}$	1 264.512 225 85(41)
		$(0\ 0\ 0)10_{4,7}$	1 550.694 389 79(36)
		$(0\ 0\ 0)10_{6,5}$	1 838.699 687 72(49)
		$(0\ 0\ 0)11_{6,5}$	2 107.810 911 90(56)

[a]The uncertainties of the last few digits are indicated in parentheses and related to the 68% confidence level. The *ortho* and *para* states are provided with their energy values relative to the $(0\ 0\ 0)0_{0,0}$ and $(0\ 0\ 0)1_{0,1}$ energies, respectively. The relative energy values of the vibrationally excited rotational states determined in this study are reported in the supplementary material.

The uncertainty due to laser-power-induced shifts, δ_{pow}, was indiscernible, i.e., below 1 kHz, during the measurements. Thus, a robust estimate of δ_{pow} = 0.5 kHz is employed for all transitions. Nonetheless, to suppress power effects, the circulating power in the cavity was lowered in those cases where possible.

As long as the vapor pressure is non-negligible within the water cell (see Fig. 1), the pressure-shift uncertainty, δ_{press}, can be significant. For eight lines, the pressure-shift effects were explicitly investigated by determining spectra over a range of pressure values (see Fig. 9). The frequency (f) of a particular transition for which pressure-dependent experiments were conducted was extrapolated to zero pressure by fitting a linear pressure-shift model,

$$f = Cp + f_{vac}, \quad (1)$$

where p is the vapor pressure applied, f_{vac} is the line frequency in vacuum, and C is the pressure-shift coefficient (slope). For those transitions recorded at multiple pressure values, δ_{press} = 0 is used, except one line, (2 0 0)$9_{5,4}$ ← (0 0 0)$8_{6,3}$, which is associated with δ_{press} = 1 kHz due to the higher (0.4 Pa) pressure applied during its observation. As the C values of these transitions were all well within the range of [−20, +15] kHz Pa^{-1}, $\delta_{press} = C_{eff}p$ is assigned to the rest of the lines, where C_{eff} = 20 kHz Pa^{-1} is the (unsigned) effective value of C and p = 0.04 Pa for most transitions. This means that δ_{press} is less than 1 kHz for all the lines. Similar to the Lamb dips[48] and Doppler-broadened[69] transitions of $H_2^{16}O$, the experimental C values of the $H_2^{18}O$ lines do not exhibit clear trends, at least not for low J values (that is, for $J \leq 11$ probed in our case), as a function of the rovibrational quantum numbers.

Three lines of the Gianfrani group,[37] claimed to be accurate to 30 kHz, were remeasured with the NICE-OHMS spectrometer, permitting one to make a direct comparison between the old and new frequency values (for details, see the footnote to Table 1). This comparison demonstrates that (a) our observations are an order of magnitude more accurate than the values of Ref. 37 and (b) the deviations of two lines are outside the uncertainty claimed in Ref. 37. The larger differences may be ascribed to the fact that the transitions of Ref. 37 were recorded at a pressure of 10 Pa, which is 250 times higher than that applied during most of our experiments (furthermore, the 15 kHz pressure-shift uncertainty given in Ref. 37 seems to be slightly optimistic in view of our C_{eff} = 20 kHz Pa^{-1} value).

As an independent verification of the frequency uncertainties and the line assignments, the NICE-OHMS transitions were closed into cycles of varying lengths. In a few cases, these cycles helped uncover that certain lines were misassigned or other mistakes were made during the experiments. The discrepancies of the cycles built from the validated transition dataset are typically on the order of 10 kHz or better, corroborating the outstanding internal consistency of the resolved lines. The fact that several transitions take part in multiple cycles further validates the accuracy of the observed lines. A couple of short cycles are drawn in Fig. 3 [panels (a)–(d)], while the cycles specified by the starred transitions of Figs. 4 and 5 are collected in the supplementary material. Note that the cycle of Fig. 3(a) exhibits a fairly small discrepancy (0.8 kHz) due to its transitions of low δ_{stat} values (well below 1 kHz). Although it may occur that these lines have sub-kHz accuracy, this assumption needs further experimental investigation and verification.

3.3. Ultraprecise relative energy values

Owing to the SNAPS design of the measurements, the ultrahigh-accuracy *para* (Fig. 4) and *ortho* (Fig. 5) lines of $H_2^{18}O$ form connected sets, allowing the determination of ultraprecise relative energies for

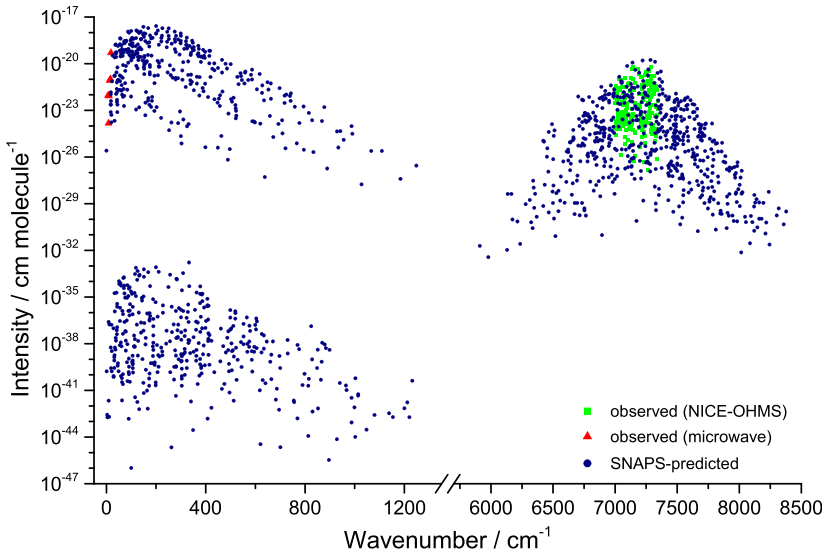

FIG. 10. Graphical representation of the high-accuracy benchmark line list of $H_2^{18}O$. The wavenumbers are calculated from the SNAPS-based relative energies of Table 2, while the one-photon, electric-dipole-allowed intensities are derived from the Einstein-A coefficients of Ref. 47. The green squares and the red triangles denote transitions observed in this study and in Ref. 13, respectively, while the blue dots correspond to SNAPS-predicted lines. In spite of the fact that the direct experimental transitions are limited to the ranges 5–15 and 7000–7350 cm^{-1}, the predicted lines extend between 0–1250 and 5900–8380 cm^{-1}. The points related to the upper left, lower left, and upper right quadrants represent $P' - P''$ = 0 − 0, 4 − 4, and 4 − 0, transitions, respectively, where P' and P'' denote the polyad numbers of the upper and lower states, respectively.

the involved *ortho* and *para* states [of course, relative to (0 0 0)$1_{0,1}$ and (0 0 0)$0_{0,0}$, respectively]. The relative energy of a rovibrational state is calculated by assembling a lowest-uncertainty path from (0 0 0)$1_{0,1}$ or (0 0 0)$0_{0,0}$ to the desired energy level and using the Ritz principle in a successive fashion. Two illustrative examples of such paths are given in Fig. 3 [see panels (e) and (f)], which specify the relative energies of the (0 0 0)$4_{2,3}$ and (0 0 0)$2_{1,1}$ states with definitive uncertainties (the full list of the utilized paths is placed in the supplementary material).

As exemplified in Fig. 3(e), the relative energies of the p^+ and o^- levels are determined by paths consisting only of NICE-OHMS transitions and running within their subcomponents. This means that the underlying energy levels are extremely well determined by the new observations. However, to derive the relative energy values of the p^- and o^+ states, the related paths should include at least one pure rotational line linking p^- with p^+ or o^+ with o^-.

While the NICE-OHMS measurements were performed to explore the relative energies of the (0 0 0)J_{K_a,K_c} states with $J \le 8$, construction of the underlying paths demanded the inclusion of several higher-J states, up to $J = 11$. These rotational energy levels, important hubs within the entire experimental SN of $H_2^{18}O$,[8] are the lower states of 16 724 lines out of the 26 696 observed transitions with distinct assignment.

The relative energies of Table 2 are highly useful to experimentalists whose desire is to utilize their spectra to derive precise relative upper-state energy values from a bunch of linear schemes [see Fig. 3(a)].[34,70] Although the uncertainties of the lower-state energies are often neglected during the analysis of these connection schemes,[34,70] they might affect significantly the accuracy of the upper-state energies deduced.[7,8]

Taking all the vibrational bands into consideration, altogether 188 energy levels are redetermined with high accuracy, of which 93, 5, 11, 35, 23, and 21 lie on the vibrational parents (0 0 0), (1 2 0), (0 2 1), (2 0 0), (1 0 1), and (0 0 2), respectively. Although the 7000–7350 cm^{-1} region includes observable lines with lower states on the (0 1 0) bending fundamental, they are not linked to the *ortho* or the *para* ground state by paths. Hence, such target lines were not selected by the SNAPS method for measurement.

The relative energy values of Table 2 have an uncertainty of 2–4 × 10^{-7} cm^{-1} for most states, while those passing through very weak lines [such as (0 0 0)$8_{8,0}$ and (0 0 0)$9_{8,2}$] are accurate to ~ 1 × 10^{-6} cm^{-1}. This accuracy, albeit based on near-infrared transitions visiting highly excited vibrational states, is at least one (but often two) order of magnitude higher than that[8] achieved via the direct traversal of the (0 0 0) pure rotational levels.[17]

3.4. Benchmark-quality reference line list

The pure rotational energies of Table 2 allow the construction of an ultrahigh-accuracy transition dataset, called benchmark line list, for both *para*- and *ortho*-$H_2^{18}O$, obeying one-photon, electric-dipole selection rules (for technical details, see Supplementary Note 6 of Ref. 48). The intensities of the lines were taken from Ref. 47. The benchmark line list, extending between 0–1250 and 5900–8380 cm^{-1}, is available in the supplementary material, and its graphical overview is shown in Fig. 10.

The benchmark line list contains 1546 transitions, about half of which are below 1250 cm^{-1}. The majority of these lines are now known with an accuracy two or even three orders of magnitude better than before.[14–23] 557 transitions are characterized by an intensity larger than 5 × 10^{-24} cm molecule^{-1}, corresponding to 1 × 10^{-26} cm molecule^{-1} by taking into account the atmospheric abundance of $H_2^{18}O$. These

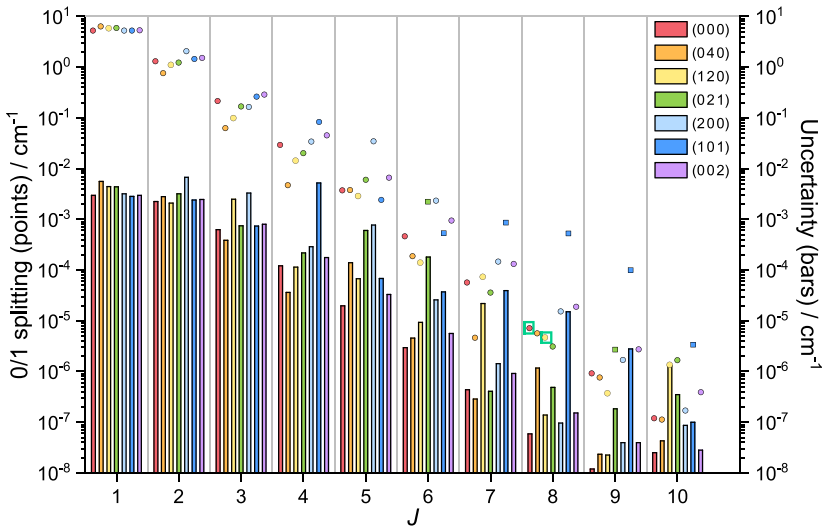

FIG. 11. Theoretical 0/1 splittings up to $J = 10$ for various vibrational bands of $H_2^{18}O$. This figure displays the 0/1 splitting values (see Sec. 2.3) obtained with the GENIUSH code.[58–60] The points denoting the 0/1 splittings are related to the left vertical axis, while the bars representing the uncertainties of the 0/1 splittings are plotted on the right vertical axis. For splittings illustrated with dots, the $K_c = 0$ energy is greater than its $K_c = 1$ pair, while for those indicated with squares, the converse relation is satisfied. The red and yellow points with a green box designate the (0 0 0)$8_{8,0/1}$ and (1 2 0)$8_{8,0/1}$ splittings, respectively, which are contained in the two paths from (0 0 0)$0_{0,0}$ to (0 0 0)$1_{0,1}$ (see Fig. 13). These two 0/1 splittings are determined to be 7.112(59) × 10^{-6} and 4.63(14) × 10^{-6} cm^{-1}, respectively.

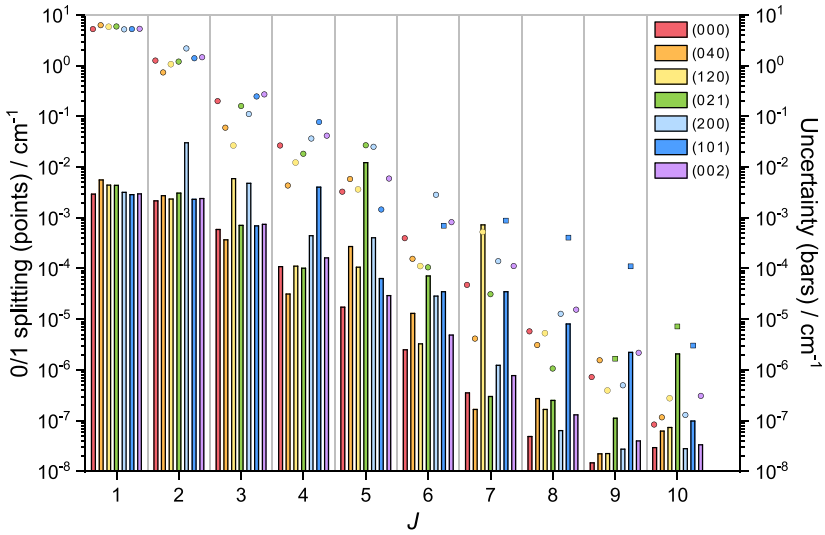

FIG. 12. Theoretical 0/1 splittings up to $J = 10$ for various vibrational bands of $H_2^{16}O$. The points and bars of this figure have the same meaning as in Fig. 11.

ultraprecise lines may serve as calibration standards for high-resolution experiments in atmospheric spectroscopy. The benchmark line list also contains 54 (mostly *ortho–para*) doublets, with separations less than 0.01 cm^{-1}; among them, there are 17 lines characterized with $S > 5 \times 10^{-24}$ cm molecule^{-1}. The 316 transitions below 1250 cm^{-1} with $S > 5 \times 10^{-24}$ cm molecule^{-1} help assess the former measurements performed in this region[14–23] and claimed to be accurate to 10^{-6}–10^{-4} cm^{-1}. Pressure-shift effects appear to lower significantly the accuracy of the previously observed lines.

3.5. Theoretical 0/1 splittings and relative doublet positions

The two states of the $(v_1\ v_2\ v_3)J_{J,0/1}$ pairs, here called 0/1 splittings, are either *ortho* or *para*. The 0/1 splittings and the relative doublet positions have been obtained through first-principles computations for a series of rovibrational states up to $J = 10$, within the ground vibrational state and the vibrational bands of the $P = 4$ polyad. For an improved comprehension of the characteristics of the 0/1 splittings, nuclear-motion computations were performed both for $H_2^{18}O$ and $H_2^{16}O$, with their results depicted in Figs. 11 and 12, respectively.

The following four PESs have been utilized: CVRQD,[61,62] including as well as excluding the diagonal Born–Oppenheimer correction (DBOC, the D part of the additively built CVRQD PES); POKAZATEL;[64] and FIS3.[63] The CVRQ(D) and POKAZATEL PESs have been developed for $H_2^{16}O$, while the FIS3 PES was designed explicitly for $H_2^{18}O$. Each computation with a specific PES was repeated with two large but sufficiently different vibrational bases, resulting in eight distinct computations. Designating a relative doublet position or a 0/1 splitting with v, its uncertainty is given as $U(v) = 2\,SD(v)$, where $SD(v)$ is the empirical standard deviation of the individual estimates for v taken from the eight computations. As the relevance of the relative doublet positions, whose values are deposited in the supplementary material, is explained in Sec. 3.1, only the 0/1 splittings are analyzed here in detail.

Upon the increase in J, the computed 0/1 splittings show a roughly exponential decrease; see Figs. 11 and 12. Splittings of 10^{-5} cm^{-1} (corresponding to 300 kHz) are reached by $J = 8$ for both water isotopologues. The uncertainties of the theoretical 0/1 splittings have to be well below 10^{-6} cm^{-1} for the network-based determination of the lowest *ortho* energy value (see Sec. 3.6). This accuracy is ensured by most 0/1 splitting values with $J \geq 8$.

The 0/1 splittings, as well as their accuracy, depend strongly on the underlying vibrational excitation. The computational inaccuracy principally originates from the PES, with gradually increasing relative uncertainties as J increases. Certain points, such as $(1\ 2\ 0)7_{7,0/1}$, do not follow the trends and/or have very large uncertainties. Furthermore, there are a few cases [namely, $(0\ 2\ 1)6_{6,0/1}$, $(0\ 2\ 1)9_{9,0/1}$, and $(1\ 0\ 1)J_{J,0/1}$ above $J = 5$ in the case of $H_2^{18}O$ and $(0\ 2\ 1)9_{9,0/1}$, $(0\ 2\ 1)10_{10,0/1}$, and $(1\ 0\ 1)J_{J,0/1}$ above $J = 5$ for $H_2^{16}O$] where the $K_c = 1$ states lie higher than their $K_c = 0$ counterparts. These anomalies are due to pronounced couplings among the vibrational parents.

Comparing Fig. 11 with Fig. 12, a very similar pattern of 0/1 splittings can be observed for $H_2^{18}O$ and $H_2^{16}O$. The rotational constants and the rotational energies of $H_2^{18}O$ are smaller than those of $H_2^{16}O$, but the 0/1 splittings can be larger for $H_2^{18}O$ than for $H_2^{16}O$. The reason behind this behavior is that these splittings depend on the differences of the rotational constants, not on their absolute values.

3.6. The lowest *ortho*-$H_2^{18}O$ energy

To transfer the accuracy of the relative *ortho* energies determined to their absolute energy values, one needs to know the energy of the lowest *ortho*-$H_2^{18}O$ state, $(0\ 0\ 0)1_{0,1}$, with a few times 10^{-7} cm^{-1} accuracy. The best literature estimates for the $(0\ 0\ 0)1_{0,1}$ energy, 23.754 902(5)[71] and 23.754 906(7)[72] cm^{-1}, are an order of magnitude

less accurate than this, implying the need for the precise redetermination of this quantity via indirect approaches.

Following the traditional spectroscopic protocol to derive the $(0\,0\,0)1_{0,1}$ energy of $H_2{}^{18}O$, an EH model was fitted to a set of energy differences on the ground vibrational state. The fitting dataset was built by joining six pure rotational lines[13] and artificial transitions formed by Λ-shape pairs [see Fig. 2(b)] of NICE-OHMS lines. From this dataset, all the lines with pure rotational *para* states with $J \leq 2$ were excluded. Since these "external" energy levels are missing from the reduced dataset, their energies serve to validate the fitted EH model below $J = 3$. The absence of the *para* ground state from the dataset implies that not only the absolute *ortho* but also the absolute *para* energies are undetermined by the reduced set. This means that one can judge the accuracy of the (lowest) absolute EH energies by analyzing the fitting residuals for the external states.

Using the reduced set of 124 transitions, a weighted least-squares fit was performed, utilizing a 49-parameter (16th-order) Watson-type Hamiltonian.[73–76] The fitting output including the optimized parameters and the fitting residuals is available in the supplementary material. The EH model yields an estimate of 23.754 904 61 cm^{-1} for the energy of the $(0\,0\,0)1_{0,1}$ state and reproduces the SNAPS-based energies of the external states perfectly, i.e., well within their uncertainty limits. Based on this observation, one can expect that the lowest *ortho* energy is similarly accurate; thus, the largest energy uncertainty of the external states, 1.9×10^{-7} cm^{-1}, is assigned as an uncertainty to the EH-predicted lowest *ortho* energy. The uncertainty for the $(0\,0\,0)1_{0,1}$ energy is ten times smaller than that of its former determinations.[71,72]

There is an independent, network-theoretical approach to extract the lowest *ortho* energy of $H_2{}^{18}O$. This approach is based on the compilation of shortest line-disjoint paths from the *para* ground state to the *ortho* one, utilizing 0/1 splittings as virtual lines. Adding all the 0/1 splittings with $J \leq 10$ to the design transition set, the SNAPS procedure returned only two such paths, both given in Fig. 13. These paths lead to two estimates for the $(0\,0\,0)1_{0,1}$ energy, 23.754 903 7(11) and 23.754 903 7(14) cm^{-1}. These values deviate by only 9.1×10^{-7} cm^{-1} from the EH estimate, which is inside their uncertainty intervals.

Owing to the long paths, going through more than 40 quantum states, and the necessary inclusion of very weak transitions in the feasible paths, with uncertainties larger than 5×10^{-7} cm^{-1}, the path-based estimates of the lowest *ortho* energy are slightly less precise than the EH value obtained. Therefore, the EH estimate, 23.754 904 61(19) cm^{-1}, is recommended as the new reference value for the lowest *ortho* energy of $H_2{}^{18}O$.

4. Conclusions and Summary

The NICE-OHMS technique,[41–45] facilitating the ultraprecise measurement of large numbers of rovibrational transitions in the near-infrared region (in the present case 7000–7350 cm^{-1}), has been used to accurately determine the entire pure rotational quantum-level

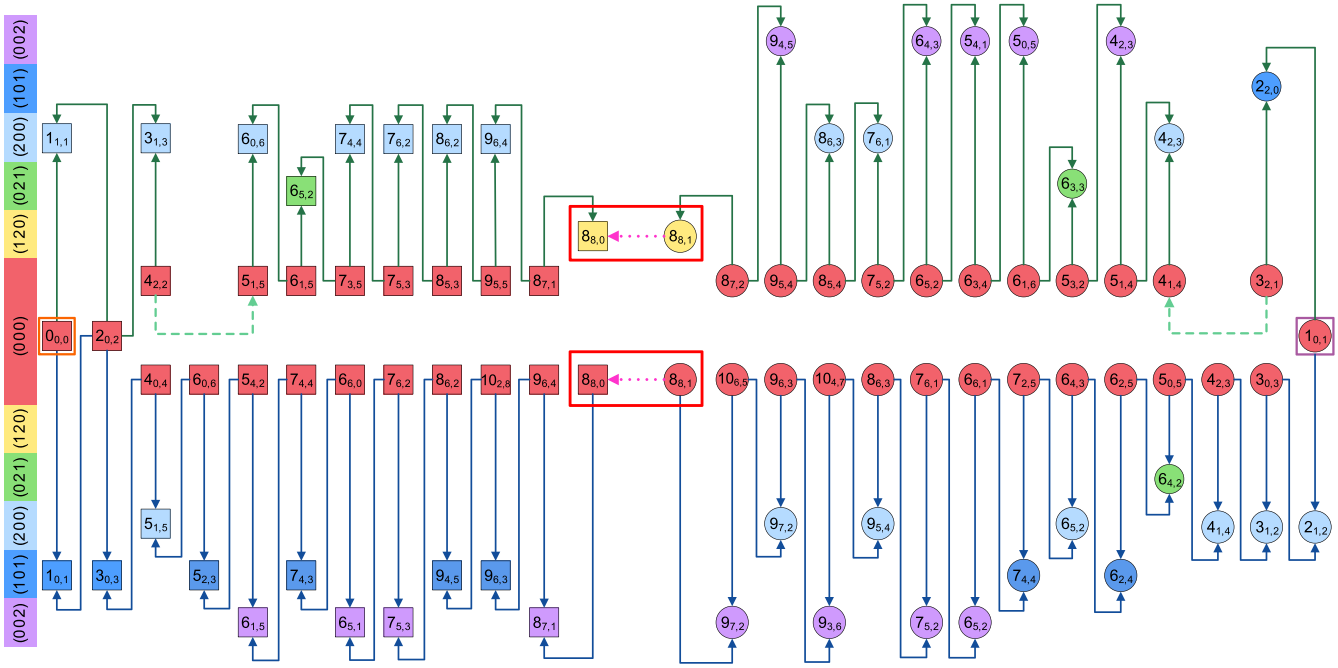

FIG. 13. Two line-disjoint paths for the determination of the lowest *ortho* energy of $H_2{}^{18}O$. The arrangement of the energy levels and the lines as well as the notation employed is similar to that of Figs. 4 and 5. Transitions of paths 1 and 2 are highlighted with green and blue arrows, respectively, while the two (light green) dashed lines are reproduced from Ref. 13. The starting and ending points of these paths, $(0\,0\,0)0_{0,0}$ and $(0\,0\,0)1_{0,1}$, are surrounded by orange and purple squares, respectively. Common states of paths 1 and 2 are positioned in the middle row of this figure. The magenta dotted lines highlighted by red frames illustrate virtual transitions whose wavenumbers are 0/1 splittings (see also the caption of Fig. 11). Invoking the Ritz principle and the law of uncertainty propagation [see the equations of Fig. 1(d)] along with the wavenumbers and uncertainties of the virtual lines, paths 1 and 2 give (by chance, numerically identical) estimates 23.754 903 7(11) and 23.754 903 7(14) cm^{-1} for the $(0\,0\,0)1_{0,1}$ energy, respectively.

structure of the second most abundant water isotopologue, $H_2^{18}O$, up to $J = 8$, where J is the rotational quantum number. These pure rotational states are often the lower states of experimental transitions in water spectroscopy;[5,6,8,9] thus, their accurate knowledge is important for a large number of applications, including some in analytical chemistry.[39] All the relative energies derived with a relative accuracy of ~10^{-11} form the basis of a benchmark line list assembled during this study, containing more than 1500 transitions. Since water is omnipresent in our universe, the entries of this line list, supplemented with a similar set of transitions for $H_2^{16}O$,[48] serve as useful references for the calibration of high-resolution spectroscopic measurements, as well as for the evaluation of the accuracy characterizing future spectral recordings in the ranges of 0–1250 and 5900–8380 cm^{-1}.

As this study proves, transferring the experimental accuracy from the near-infrared to the microwave and mid-infrared region is possible by taking advantage of the results of advanced quantum-chemical computations[57] and the design principles of the SNAPS scheme.[48] SNAPS is an intelligent and universally applicable network-theory-based protocol able to provide connected sets of transitions, forming paths and cycles in the language of network theory, possible targets of ultraprecise observations. Furthermore, SNAPS helps evaluate the utility of and the possible discrepancies related to newly probed lines. During this study, the original SNAPS approach[48] was extended with a novel feature, the so-called Λ-correction scheme, accelerating the detection of extremely weak transitions. SNAPS is a particularly useful tool for ultrahigh-resolution laser spectroscopists trying to survey spectroscopic features of isolated molecules of chemical interest with the highest possible efficiency.

Among the 195 carefully selected near-infrared Lamb-dip lines of $H_2^{18}O$ recorded during this study, the unparalleled instrumental characteristics (resolution, accuracy, and sensitivity) of the NICE-OHMS setup allowed us to resolve transitions that cannot be probed under ordinary (e.g., Doppler-limited) experimental conditions, such as *ortho–para* doublets. The sensitivity of the NICE-OHMS technique also means that lines observed also include those of disturbing species, such as $H_2^{16}O$ and $HD^{18}O$, present in a tiny fraction of the sample. Notably, the Lamb-dip profiles of the disturbing $H_2^{16}O$ and $HD^{18}O$ lines are quite similar to those typical of the $H_2^{18}O$ transitions, making their confusion rather easy. Nevertheless, the SNAPS cycles constructed during this study and the relatively large deviations from an EH model help reveal if a resolved line is not the one searched for.

Appropriate resolution of extremely weak transitions required technical improvements, allowing dependable averaging of multiple scans. The measurements were also helped by the introduction of the Λ-correction scheme mentioned, providing accurate initial positions and enabling narrow-range frequency scans. In 2020, Wu and coworkers[77] stated that the weakest transition that has ever been measured in saturation is their CO_2 line with $S = 6 \times 10^{-27}$ cm molecule^{-1}. In this study, a four times weaker transition, with an intensity of $S = 1.4 \times 10^{-27}$ cm molecule^{-1}, could be observed with a reasonable accuracy of 25 kHz. These studies pave the way to the detection of even weaker transitions, such as quadrupole lines. Such quadrupole lines of water have recently been detected in Doppler-broadened spectroscopy,[78,79] but not in saturation and not with the expected accuracy of NICE-OHMS measurements.

Linking the parity-related subcomponents formed by electric-dipole-allowed transitions measured by NICE-OHMS of the nuclear-spin isomers, *para* and *ortho*, of $H_2^{18}O$ required the utilization of accurate rotational lines taken from the literature.[13] It would be highly useful to record quadrupole-allowed lines via NICE-OHMS to establish ultraprecise connections between the appropriate subcomponents. These experiments would further validate the accuracy of microwave transitions, for example, those of Ref. 13. Since these quadrupole lines have room-temperature intensities on the order of 10^{-28} cm molecule^{-1},[78,79] their observation demands further technical improvements of our NICE-OHMS spectrometer.

To ensure maximum accuracy, a detailed uncertainty analysis of the line positions was conducted, including the evaluation of the short- and long-term reproducibility of the measurements. By keeping the pressure at a remarkably low level, around 0.04 Pa in most cases, an average experimental accuracy of 2.5 kHz is reached, which is even superior to that of our previous study on $H_2^{16}O$.[48] Experiments aimed at establishing the effect of sample pressure on the recorded lines suggest that the transitions of $H_2^{16}O$ (see Ref. 48) and $H_2^{18}O$ behave similarly against pressure variation and that the pressure dependence of certain line centers is significantly higher than that claimed in Ref. 38.

To convert the relative energies of this study to absolute energies for *ortho*-$H_2^{18}O$, its lowest energy had to be derived. This was achieved both via an EH fit and by a network-theoretical approach based on paths, involving small but highly accurate quantum-chemically computed *ortho–para* energy splittings as virtual transitions. As a result of this study, many more accurate rotational energies are available than before. The EH-based estimate for the lowest *ortho*-$H_2^{18}O$ energy, 23.754 904 61(19) cm^{-1}, has a smaller uncertainty than those of its previous determinations. The large number of accurate absolute energies provides benchmarks for quantum-chemical computations, helps improve the accuracy of thermochemical functions at low temperatures, and is important for modelers, for example, of (exo) planetary atmospheres.

The *ortho–para* doublet separations extracted from quantum-chemical computations can be compared directly with the present ultraprecise NICE-OHMS observations. Due to significant error compensation when differences of certain rovibrational energies are formed, this comparison reveals excellent agreement between the computed and the observed separations. Although assigning the lines of the doublets is trivial due to the (1:3) dip ratios, the predicted doublet separations helped uncover accidental misassignments and calibration errors. The absolute and relative doublet positions provide benchmarks for those who would like to improve the sensitivity and resolution of their spectrometers.

The transitions detailed in the benchmark line list yielded by this study are now known with an accuracy two to three orders of magnitude better than before. Thus, it is important to discuss how this knowledge affects entries of existing line-by-line (LBL) databanks, such as HITRAN.[9] First, replacement of existing transition records would be particularly beneficial in the case of the 557 lines characterized by room-temperature absorption intensities larger than 5×10^{-24} cm molecule^{-1} because all of these transitions are highly relevant to atmospheric modeling. Second, while the pressure dependence of certain $H_2^{18}O$ lines has been explicitly determined during this study, it is not clear how the pressure-shift coefficients revealed could be utilized to improve the related entries of LBL databases.

Third, the pure rotational states, whose relative energies are accurately derived via the SNAPS scheme, are among the most important hubs in the entire experimental SN of $H_2^{18}O$; they are the lower states of a large number of transitions. Therefore, consideration of these ultraprecise pure rotational energy values may help eliminate systematic errors during the determination of upper-state energies of LBL datasets.

5. Supplementary Material

See the supplementary material for the list of experimental transitions recorded with the NICE-OHMS technique (Table S1); the list of experimental transitions taken from Ref. 13 (Table S2); the predicted line list and the relative rovibrational energies derived during this study (Tables S3 and S4, respectively); the output of the EH fit (Table S5); two line-disjoint paths for the derivation of the lowest *ortho* energy of $H_2^{18}O$ (Table S6); quantum-chemical 0/1 splittings, up to $J = 10$, for $H_2^{16}O$ and $H_2^{18}O$ (Table S7); the comparison of the quantum-chemical doublet separations with their experimental counterparts (Table S8); and basic cycles associated with the shortest-path-based forest of the SN built upon by lines of Ref. 13 and this study (Table S9).

Acknowledgments

This research received funding from LASERLAB-EUROPE (Grant No. 654148), a European Union's Horizon 2020 research and innovation programme. The work performed in Budapest received support from NKFIH (Grant No. K119658), from the grant VEKOP-2.3.2-16-2017-000, and from the ELTE Institutional Excellence Program (Grant No. TKP2020-IKA-05) financed by the Hungarian Ministry of Human Capacities. W.U. acknowledges the European Research Council for an ERC Advanced Grant (Grant No. 670168). Further support was obtained from a NWO-FOM program (Grant No. 16MYSTP) and from the NWO Dutch Astrochemistry Network.

Data Availability

The data that support the findings of this study are available within the article and its supplementary material.

6. References

[1]P. F. Bernath, "The spectroscopy of water vapour: Experiment, theory and applications," Phys. Chem. Chem. Phys. **4**, 1501 (2002).

[2]J. Tennyson, P. F. Bernath, L. R. Brown, A. Campargue, M. R. Carleer, A. G. Császár, R. R. Gamache, J. T. Hodges, A. Jenouvrier, O. V. Naumenko, O. L. Polyansky, L. S. Rothman, R. A. Toth, A. C. Vandaele, N. F. Zobov, L. Daumont, A. Z. Fazliev, T. Furtenbacher, I. E. Gordon, S. N. Mikhailenko, and S. V. Shirin, "IUPAC critical evaluation of the rotational–vibrational spectra of water vapor. Part I. Energy levels and transition wavenumbers for $H_2^{17}O$ and $H_2^{18}O$," J. Quant. Spectrosc. Radiat. Transfer **110**, 573 (2009).

[3]J. Tennyson, P. F. Bernath, L. R. Brown, A. Campargue, A. G. Császár, L. Daumont, R. R. Gamache, J. T. Hodges, O. V. Naumenko, O. L. Polyansky, L. S. Rothman, R. A. Toth, A. C. Vandaele, N. F. Zobov, S. Fally, A. Z. Fazliev, T. Furtenbacher, I. E. Gordon, S.-M. Hu, S. N. Mikhailenko, and B. A. Voronin, "IUPAC critical evaluation of the rotational–vibrational spectra of water vapor. Part II. Energy levels and transition wavenumbers for $HD^{16}O$, $HD^{17}O$, and $HD^{18}O$," J. Quant. Spectrosc. Radiat. Transfer **111**, 2160 (2010).

[4]J. Tennyson, P. F. Bernath, L. R. Brown, A. Campargue, A. G. Császár, L. Daumont, R. R. Gamache, J. T. Hodges, O. V. Naumenko, O. L. Polyansky, L. S. Rothman, A. C. Vandaele, N. F. Zobov, A. R. Al Derzi, C. Fábri, A. Z. Fazliev, T. Furtenbacher, I. E. Gordon, L. Lodi, and I. I. Mizus, "IUPAC critical evaluation of the rotational–vibrational spectra of water vapor. Part III. Energy levels and transition wavenumbers for $H_2^{16}O$," J. Quant. Spectrosc. Radiat. Transfer **117**, 29 (2013).

[5]J. Tennyson, P. F. Bernath, L. R. Brown, A. Campargue, A. G. Császár, L. Daumont, R. R. Gamache, J. T. Hodges, O. V. Naumenko, O. L. Polyansky, L. S. Rothman, A. C. Vandaele, N. F. Zobov, N. Dénes, A. Z. Fazliev, T. Furtenbacher, I. E. Gordon, S.-M. Hu, T. Szidarovszky, and I. A. Vasilenko, "IUPAC critical evaluation of the rotational–vibrational spectra of water vapor. Part IV. Energy levels and transition wavenumbers for $D_2^{16}O$, $D_2^{17}O$, and $D_2^{18}O$," J. Quant. Spectrosc. Radiat. Transfer **142**, 93 (2014).

[6]J. Tennyson, P. F. Bernath, L. R. Brown, A. Campargue, A. G. Császár, L. Daumont, R. R. Gamache, J. T. Hodges, O. V. Naumenko, O. L. Polyansky, L. S. Rothman, A. C. Vandaele, and N. F. Zobov, "A database of water transitions from experiment and theory (IUPAC technical report)," Pure Appl. Chem. **86**, 71 (2014).

[7]T. Furtenbacher, R. Tóbiás, J. Tennyson, O. L. Polyansky, and A. G. Császár, "W2020: A database of validated rovibrational experimental transitions and empirical energy levels of $H_2^{16}O$," J. Phys. Chem. Ref. Data **49**, 033101 (2020).

[8]T. Furtenbacher, R. Tóbiás, J. Tennyson, O. L. Polyansky, A. A. Kyuberis, R. I. Ovsyannikov, N. F. Zobov, and A. G. Császár, "The W2020 database of validated rovibrational experimental transitions and empirical energy levels of water isotopologues. Part II. $H_2^{17}O$ and $H_2^{18}O$ with an update to $H_2^{16}O$," J. Phys. Chem. Ref. Data **49**, 043103 (2020).

[9]I. E. Gordon, L. S. Rothman, C. Hill, R. V. Kochanov, Y. Tan, P. F. Bernath, M. Birk, V. Boudon, A. Campargue, K. V. Chance, B. J. Drouin, J.-M. Flaud, R. R. Gamache, J. T. Hodges, D. Jacquemart, V. I. Perevalov, A. Perrin, K. P. Shine, M.-A. H. Smith, J. Tennyson, G. C. Toon, H. Tran, V. G. Tyuterev, A. Barbe, A. G. Császár, V. M. Devi, T. Furtenbacher, J. J. Harrison, J.-M. Hartmann, A. Jolly, T. J. Johnson, T. Karman, I. Kleiner, A. A. Kyuberis, J. Loos, O. M. Lyulin, S. T. Massie, S. N. Mikhailenko, N. Moazzen-Ahmadi, H. S. P. Müller, O. V. Naumenko, A. V. Nikitin, O. L. Polyansky, M. Rey, M. Rotger, S. W. Sharpe, K. Sung, E. Starikova, S. A. Tashkun, J. V. Auwera, G. Wagner, J. Wilzewski, P. Wcisło, S. Yu, and E. J. Zak, "The HITRAN 2016 molecular spectroscopic database," J. Quant. Spectrosc. Radiat. Transfer **203**, 3 (2017).

[10]E. González-Alfonso, J. Fischer, J. Graciá-Carpio, E. Sturm, S. Hailey-Dunsheath, D. Lutz, A. Poglitsch, A. Contursi, H. Feuchtgruber, S. Veilleux, H. W. W. Spoon, A. Verma, N. Christopher, R. Davies, A. Sternberg, R. Genzel, and L. Tacconi, "*Herschel*/PACS spectroscopy of NGC 4418 and Arp 220: H_2O, $H_2^{18}O$, OH, ^{18}OH, O I, HCN, and NH_3," Astron. Astrophys. **541**, A4 (2012).

[11]F. X. Powell and D. R. Johnson, "Microwave detection of $H_2^{18}O$," Phys. Rev. Lett. **24**, 637 (1970).

[12]G. Steenbeckeliers and J. Bellet, "Spectre micro-onde de molecules $H_2^{16}O$, $H_2^{17}O$ et $H_2^{18}O$," C. R. Acad. Sci., Ser. B **273**, 471 (1971).

[13]G. Y. Golubiatnikov, V. N. Markov, A. Guarnieri, and R. Knöchel, "Hyperfine structure of $H_2^{16}O$ and $H_2^{18}O$ measured by Lamb-dip technique in the 180–560 GHz frequency range," J. Mol. Spectrosc. **240**, 251 (2006).

[14]F. C. de Lucia, P. Helminger, R. L. Cook, and W. Gordy, "Submillimeter microwave spectrum of $H_2^{18}O$," Phys. Rev. A **6**, 1324 (1972).

[15]R. H. Partridge, "Far-infrared absorption spectra of $H_2^{16}O$, $H_2^{17}O$, and $H_2^{18}O$," J. Mol. Spectrosc. **87**, 429 (1981).

[16]S. P. Belov, I. N. Kozin, O. L. Polyansky, M. Y. Tret'yakov, and N. F. Zobov, "Rotational spectrum of the $H_2^{16}O$ molecule in the (0 1 0) excited vibrational state," J. Mol. Spectrosc. **126**, 113 (1987).

[17]F. Matsushima, H. Nagase, T. Nakauchi, H. Odashima, and K. Takagi, "Frequency measurement of pure rotational transitions of $H_2^{17}O$ and $H_2^{18}O$ from 0.5 to 5 THz," J. Mol. Spectrosc. **193**, 217 (1999).

[18]J. Kauppinen, T. Kärkkäinen, and E. Kyrö, "High-resolution spectrum of water vapour between 30 and 720 cm^{-1}," J. Mol. Spectrosc. **71**, 15 (1978).

[19]J. Kauppinen and E. Kyrö, "High resolution pure rotational spectrum of water vapor enriched by $H_2^{17}O$ and $H_2^{18}O$," J. Mol. Spectrosc. **84**, 405 (1980).

[20]J. W. C. Johns, "High-resolution far-infrared (20–350 cm^{-1}) spectra of several isotopic species of H_2O," J. Opt. Soc. Am. B **2**, 1340 (1985).

[21]R. A. Toth, "Water vapor measurements between 590 and 2582 cm^{-1}: Line positions and strengths," J. Mol. Spectrosc. **190**, 379 (1998).

[22]S. N. Mikhailenko, V. G. Tyuterev, and G. Mellau, "(0 0 0) and (0 1 0) states of $H_2{}^{18}O$: Analysis of rotational transitions in hot emission spectrum in the 400–850 cm^{-1} region," J. Mol. Spectrosc. **217**, 195 (2003).
[23]S. N. Mikhailenko, S. Béguier, T. A. Odintsova, M. Y. Tretyakov, O. Pirali, and A. Campargue, "The far-infrared spectrum of ^{18}O enriched water vapour (40–700 cm^{-1})," J. Quant. Spectrosc. Radiat. Transfer **253**, 107105 (2020).
[24]G. Guelachvili, "Experimental Doppler-limited spectra of the ν_2-bands of $H_2{}^{16}O$, $H_2{}^{17}O$, $H_2{}^{18}O$, and HDO by Fourier-transform spectroscopy-secondary wavenumber standards between 1066 and 2296 cm^{-1}," J. Opt. Soc. Am. **73**, 137 (1983).
[25]J.-P. Chevillard, J.-Y. Mandin, J.-M. Flaud, and C. Camy-Peyret, "$H_2{}^{16}O$: Line positions and intensities between 9500 and 11500 cm^{-1}. The (041), (220), (121), (300), (201), (102) and (003) interacting states," Can. J. Phys. **65**, 777 (1987).
[26]A. Bykov, O. Naumenko, T. Petrova, A. Scherbakov, L. Sinitsa, J. Y. Mandin, C. Camypeyret, and J. M. Flaud, "The second decade of $H_2{}^{18}O$: Line positions and energy levels," J. Mol. Spectrosc. **172**, 243 (1995).
[27]M. Tanaka, O. Naumenko, J. W. Brault, and J. Tennyson, "Fourier transform absorption spectra of $H_2{}^{18}O$ and $H_2{}^{17}O$ in the $3\nu + \delta$ and 4ν polyad region," J. Mol. Spectrosc. **234**, 1 (2005).
[28]A.-W. Liu, J.-H. Du, K.-F. Song, L. Wang, L. Wan, and S.-M. Hu, "High-resolution Fourier-transform spectroscopy of ^{18}O-enriched water molecule in the 1080–7800 cm^{-1} region," J. Mol. Spectrosc. **237**, 149 (2006).
[29]C. Oudot, L. Régalia, S. Mikhailenko, X. Thomas, P. von der Heyden, and D. Décatoire, "Fourier transform measurements of $H_2{}^{18}O$ and $HD^{18}O$ in the spectral range 1000–2300 cm^{-1}," J. Quant. Spectrosc. Radiat. Transfer **113**, 859 (2012).
[30]F. Mazzotti, R. N. Tolchenov, and A. Campargue, "High sensitivity ICLAS of $H_2{}^{18}O$ in the region of the second decade (11 520–12 810 cm^{-1})," J. Mol. Spectrosc. **243**, 78 (2007).
[31]O. M. Leshchishina, O. V. Naumenko, and A. Campargue, "High sensitivity ICLAS of $H_2{}^{18}O$ between 13 540 and 14 100 cm^{-1}," J. Mol. Spectrosc. **268**, 28 (2011).
[32]J. L. Hall, "Nobel lecture: Defining and measuring optical frequencies," Rev. Mod. Phys. **78**, 1279 (2006).
[33]T. W. Hänsch, "Nobel lecture: Passion for precision," Rev. Mod. Phys. **78**, 1297 (2006).
[34]J. Chen, T.-P. Hua, L.-G. Tao, Y. R. Sun, A.-W. Liu, and S.-M. Hu, "Absolute frequencies of water lines near 790 nm with 10^{-11} accuracy," J. Quant. Spectrosc. Radiat. Transfer **205**, 91 (2018).
[35]Z. D. Reed, D. A. Long, H. Fleurbaey, and J. T. Hodges, "SI-traceable molecular transition frequency measurements at the 10^{-12} relative uncertainty level," Optica **7**, 1209 (2020).
[36]Z. D. Reed, B. J. Drouin, D. A. Long, and J. T. Hodges, "Molecular transition frequencies of CO_2 near 1.6 μm with kHz-level uncertainties," J. Quant. Spectrosc. Radiat. Transfer **271**, 107681 (2021).
[37]A. Gambetta, E. Fasci, A. Castrillo, M. Marangoni, G. Galzerano, G. Casa, P. Laporta, and L. Gianfrani, "Frequency metrology in the near-infrared spectrum of $H_2{}^{17}O$ and $H_2{}^{18}O$ molecules: Testing a new inversion method for retrieval of energy levels," New J. Phys. **12**, 103006 (2010).
[38]G. Galzerano, A. Gambetta, E. Fasci, A. Castrillo, M. Marangoni, P. Laporta, and L. Gianfrani, "Absolute frequency measurement of a water-stabilized diode laser at 1.384 μm by means of a fiber frequency comb," Appl. Phys. B **102**, 725 (2011).
[39]A. Maity, S. Maithani, and M. Pradhan, "Cavity ring-down spectroscopy: Recent technological advancements, techniques, and applications," Anal. Chem. **93**, 388 (2021).
[40]J. C. Visschers, E. Wilson, T. Conneely, A. Mudrov, and L. Bougas, "Rapid parameter determination of discrete damped sinusoidal oscillations," Opt. Express **29**, 6863 (2021).
[41]L.-S. Ma, J. Ye, P. Dubé, and J. L. Hall, "Ultrasensitive frequency-modulation spectroscopy enhanced by a high-finesse optical cavity: Theory and application to overtone transitions of C_2H_2 and C_2HD," J. Opt. Soc. Am. B **16**, 2255 (1999).
[42]A. Foltynowicz, F. M. Schmidt, W. Ma, and O. Axner, "Noise-immune cavity-enhanced optical heterodyne molecular spectroscopy: Current status and future potential," Appl. Phys. B **92**, 313 (2008).
[43]S. Twagirayezu, M. J. Cich, T. J. Sears, C. P. McRaven, and G. E. Hall, "Frequency-comb referenced spectroscopy of ν_4- and ν_5-excited hot bands in the 1.5 μm spectrum of C_2H_2," J. Mol. Spectrosc. **316**, 64 (2015).
[44]F. M. J. Cozijn, P. Dupré, E. J. Salumbides, K. S. E. Eikema, and W. Ubachs, "Sub-Doppler frequency metrology in HD for tests of fundamental physics," Phys. Rev. Lett. **120**, 153002 (2018).
[45]T. P. Hua, Y. R. Sun, J. Wang, A. W. Liu, and S. M. Hu, "Frequency metrology of molecules in the near-infrared by NICE-OHMS," Opt. Express **27**, 6106 (2019).
[46]L. Lodi and J. Tennyson, "Line lists for $H_2{}^{18}O$ and $H_2{}^{17}O$ based on empirical line positions and *ab initio* intensities," J. Quant. Spectrosc. Radiat. Transfer **113**, 850 (2012).
[47]O. L. Polyansky, A. A. Kyuberis, L. Lodi, J. Tennyson, R. I. Ovsyannikov, and N. Zobov, "ExoMol molecular line lists XIX: High accuracy computed line lists for $H_2{}^{17}O$ and $H_2{}^{18}O$," Mon. Not. R. Astron. Soc. **466**, 1363 (2017).
[48]R. Tóbiás, T. Furtenbacher, I. Simkó, A. G. Császár, M. L. Diouf, F. M. J. Cozijn, J. M. A. Staa, E. J. Salumbides, and W. Ubachs, "Spectroscopic-network-assisted precision spectroscopy and its application to water," Nat. Commun. **11**, 1708 (2020).
[49]A. G. Császár and T. Furtenbacher, "Spectroscopic networks," J. Mol. Spectrosc. **266**, 99 (2011).
[50]T. Furtenbacher and A. G. Császár, "MARVEL: Measured active rotational-vibrational energy levels. II. Algorithmic improvements," J. Quant. Spectrosc. Radiat. Transfer **113**, 929 (2012).
[51]T. Furtenbacher, P. Árendás, G. Mellau, and A. G. Császár, "Simple molecules as complex systems," Sci. Rep. **4**, 4654 (2014).
[52]A. G. Császár, T. Furtenbacher, and P. Árendás, "Small molecules—Big data," J. Phys. Chem. A **120**, 8949 (2016).
[53]R. S. Mulliken, "Report on notation for the spectra of polyatomic molecules," J. Chem. Phys. **23**, 1997 (1955).
[54]H. W. Kroto, *Molecular Rotation Spectra* (Dover, New York, 1992).
[55]R. J. Barber, J. Tennyson, G. J. Harris, and R. N. Tolchenov, "A high-accuracy computed water line list," Mon. Not. R. Astron. Soc. **368**, 1087 (2006).
[56]A. Miani and J. Tennyson, "Can *ortho–para* transitions for water be observed?," J. Chem. Phys. **120**, 2732 (2004).
[57]A. G. Császár, C. Fábri, T. Szidarovszky, E. Mátyus, T. Furtenbacher, and G. Czakó, "The fourth age of quantum chemistry: Molecules in motion," Phys. Chem. Chem. Phys. **14**, 1085 (2012).
[58]C. Fábri, M. Quack, and A. G. Császár, "On the use of nonrigid-molecular symmetry in nuclear-motion computations employing a discrete variable representation: A case study of the bending energy levels of CH_5^+," J. Chem. Phys. **147**, 134101 (2017).
[59]E. Mátyus, G. Czakó, and A. G. Császár, "Toward black-box-type full- and reduced-dimensional variational (ro)vibrational computations," J. Chem. Phys. **130**, 134112 (2009).
[60]C. Fábri, E. Mátyus, and A. G. Császár, "Rotating full- and reduced-dimensional quantum chemical models of molecules," J. Chem. Phys. **134**, 074105 (2011).
[61]O. L. Polyansky, A. G. Császár, S. V. Shirin, N. F. Zobov, P. Barletta, J. Tennyson, D. W. Schwenke, and P. J. Knowles, "High-accuracy *ab initio* rotation–vibration transitions for water," Science **299**, 539 (2003).
[62]P. Barletta, S. V. Shirin, N. F. Zobov, O. L. Polyansky, J. Tennyson, E. F. Valeev, and A. G. Császár, "CVRQD *ab initio* ground-state adiabatic potential energy surfaces for the water molecule," J. Chem. Phys. **125**, 204307 (2006).
[63]S. V. Shirin, O. L. Polyansky, N. F. Zobov, R. I. Ovsyannikov, A. G. Császár, and J. Tennyson, "Spectroscopically determined potential energy surfaces of the $H_2{}^{16}O$, $H_2{}^{17}O$ and $H_2{}^{18}O$ isotopologues of water," J. Mol. Spectrosc. **236**, 216 (2006).
[64]O. L. Polyansky, A. A. Kyuberis, N. F. Zobov, J. Tennyson, S. N. Yurchenko, and L. Lodi, "ExoMol molecular line lists XXX: A complete high-accuracy line list for water," Mon. Not. R. Astron. Soc. **480**, 2597 (2018).
[65]A.-W. Liu, O. Naumenko, K.-F. Song, B. Voronin, and S.-M. Hu, "Fourier-transform absorption spectroscopy of $H_2{}^{18}O$ in the first hexade region," J. Mol. Spectrosc. **236**, 127 (2006).
[66]O. Leshchishina, S. Mikhailenko, D. Mondelain, S. Kassi, and A. Campargue, "CRDS of water vapor at 0.1 Torr between 6886 and 7406 cm^{-1}," J. Quant. Spectrosc. Radiat. Transfer **113**, 2155 (2012).
[67]S. N. Mikhailenko, D. Mondelain, E. V. Karlovets, S. Kassi, and A. Campargue, "Comb-assisted cavity ring down spectroscopy of ^{17}O enriched water between 6667 and 7443 cm^{-1}," J. Quant. Spectrosc. Radiat. Transfer **206**, 163 (2018).

[68]L. Régalia, X. Thomas, T. Rennesson, and S. Mikhailenko, "Line parameters of water vapor enriched by ^{18}O from 6525 to 8011 cm^{-1}," J. Quant. Spectrosc. Radiat. Transfer **235**, 257 (2019).

[69]Q. Ma, R. H. Tipping, and N. N. Lavrentieva, "Pair identity and smooth variation rules applicable for the spectroscopic parameters of H_2O transitions involving high-J states," Mol. Phys. **109**, 1925 (2011).

[70]S. N. Mikhailenko, S. Kassi, D. Mondelain, and A. Campargue, "Water vapor absorption between 5690 and 8340 cm^{-1}: Accurate empirical line centers and validation tests of calculated line intensities," J. Quant. Spectrosc. Radiat. Transfer **245**, 106840 (2020).

[71]R. A. Toth, "Transition frequencies and absolute strengths of $H_2{}^{17}O$ and $H_2{}^{18}O$ in the 6.2-μm region," J. Opt. Soc. Am. B **9**, 462 (1992).

[72]See https://spec.jpl.nasa.gov/ftp/pub/catalog/archive/c020003.egy for JPL website.

[73]J. K. G. Watson, "Determination of centrifugal distortion coefficients of asymmetric-top molecules," J. Chem. Phys. **46**, 1935 (1967).

[74]J. K. G. Watson, "Simplification of the molecular vibration–rotation Hamiltonian," Mol. Phys. **15**, 479 (1968).

[75]J. K. G. Watson, "Determination of centrifugal distortion coefficients of asymmetric-top molecules. II. Dreizler, Drendl, and Rudolph's results," J. Chem. Phys. **48**, 181 (1968).

[76]J. K. G. Watson, "Determination of centrifugal distortion coefficients of asymmetric-top molecules. III. Sextic coefficients," J. Chem. Phys. **48**, 4517 (1968).

[77]H. Wu, C.-L. Hu, J. Wang, Y. R. Sun, Y. Tan, A.-W. Liu, and S.-M. Hu, "A well-isolated vibrational state of CO_2 verified by near-infrared saturated spectroscopy with kHz accuracy," Phys. Chem. Chem. Phys. **22**, 2841 (2020).

[78]A. Campargue, A. M. Solodov, A. A. Solodov, A. Yachmenev, and S. N. Yurchenko, "Detection of electric-quadrupole transitions in water vapour near 5.4 and 2.5 μm," Phys. Chem. Chem. Phys. **22**, 12476 (2020).

[79]A. Campargue, S. Kassi, A. Yachmenev, A. A. Kyuberis, J. Küpper, and S. N. Yurchenko, "Observation of electric-quadrupole infrared transitions in water vapor," Phys. Rev. Res. **2**, 023091 (2020).